A Simple Method for Correcting Empirical Model Densities during Geomagnetic Storms Using Satellite Orbit Data

Daniel A.Brandt[1], Charles D. Bussy-Virat[1], Aaron J. Ridley[1]

[1]Department of Climate and Space Sciences and Engineering, University of Michigan, Ann Arbor, MI, USA

Key Points:

- There exists a lack of thermospheric density measurements, especially during storms, when empirical models typically underperform.
- From two-line elements describing satellite orbits, the density can be determined using a newly-developed Multifaceted Optimization Algorithm.
- The technique is validated against SWARM densities derived during geomagnetic quiet and active times.

Corresponding author: D. A. Brandt, branddan@umich.edu

Abstract

Empirical models of the thermospheric neutral density are routinely used by mission planners and systems engineers to perform orbit maintenance, collision avoidance, and estimate time and location of re-entry for spacecraft. These models have characteristic errors in neutral density below 10% during geomagnetic quiet time, but perform worse during intense geomagnetic activity, being unable to reproduce the significant increases in the neutral density that are observed during geomagnetic storms. Underestimation of the density during these conditions translates to errors in orbit propagation that reduce the accuracy of any resulting orbit predictions. These drawbacks directly translate into safety risks for astronauts and orbiting spacecraft, but also limit our understanding of the physics of neutral density enhancements. Numerous CubeSats with publicly available ephemeris in the form of two-line element (TLEs) sets orbit in this region. We present the Multifaceted Optimization Algorithm (MOA), a method to estimate the neutral density by minimizing the error between a modeled trajectory and a set of TLEs. Specifically, the algorithm estimates corrections to the inputs of the NRLMSISE-00 empirical density model, and applies those corrections along-track the SWARM spacecraft orbits. This results in orbit-averaged empirical densities below 10% error in magnitude, compared to errors in excess of 25% for uncalibrated NLRMSISE-00.

Plain Language Summary

Empirical atmospheric density models underestimate the increase in thermosphere's neutral density observed during times of intense solar and geomagnetic activity. This demonstrates our limited understanding of the physics of the thermosphere during these times, and limits our ability to accurately predict the orbits of both operational satellites and space debris. We present a method to correct these density underestimations by using an orbital propagator and correcting the inputs to the NRLMSISE-00 density model to minimize orbit error. We apply medians of these corrections along the orbit of the SWARM spacecraft and compare the resulting corrected densities to densities collected by SWARM.

1 Introduction

Earth's thermosphere is the region of the atmosphere between approximately 90 km and 800 km, depending on solar conditions. Its middle and upper regions are the abode of numerous Low-Earth Orbiting (LEO) satellites that constitute billions of dollars in assets and are accompanied by some 20,000 currently known and trackable objects of space debris at least the size of a softball (Johnson, 1993). Understanding the behavior of the density of this region is vital to being able to accurately predict the orbits of these objects, as the amount of drag they experience is contingent on the magnitude of the local neutral density. Empirical models of the thermosphere like Jacchia-1972 (Jacchia, 1979), DTM-2012 (S. Bruinsma et al., 2003), and NLRMSISE-00 (Picone et al., 2002) are used by the space situational awareness community to estimate the thermospheric density for orbit prediction. These models commonly exhibit errors in the density in excess of 20% during periods of high geomagnetic activity (Burke et al. (2007), Liu et al. (2005)). Density errors translate directly into orbit errors, jeopardizing the success of collision avoidance, re-entry prediction, and spacecraft manoeuvre planning (Bussy-Virat, Ridley, and Getchius (2018), Doornbos and Klinkrad (2006))

It is understood that the thermosphere's state is highly contingent on the energy input it receives in the form of Solar EUV, Joule/frictional heating, and auroral precipitation, which all serve to control the thermospheric temperature. During nominal geomagnetic activity, incoming solar EUV constitutes the largest part of the thermosphere's energy budget, but during a geomagnetic storm, up to two-thirds of the energy budget can be comprised by Joule/frictional heating and auroral precipitation (Knipp et al., 2004). The direct dependence of the neutral density on the temperature results in the dynam-

ics of the thermospheric density being influenced by geomagnetic activity diurnal tides, solar rotation, and the solar cycle (Forbes et al. (2012), Rhoden et al. (2000), Ruan et al. (2015), Vickers et al. (2014)).

The second largest source of energy into the thermosphere is high-latitude Joule (or frictional) heating. This is due to collisions between ions and neutrals, since these populations have differing bulk velocities and temperatures. During quiet times, the Joule heating is relatively small compared to the solar EUV, but during geomagnetic storms, the heating at high latitudes can become the dominant source of energy into the thermosphere, causing up to an 800% increase in the density as up to 1000 GW of energy is deposited during the storm (Liu and Lhr (2005), Sutton et al. (2009), and Vichare and Lakhina (2005)). Variations in the thermospheric density due to thermal expansion from EUV radiation and Joule heating affect orbiting satellites by changing the degree of atmospheric drag they experience as energy from high latitudes is distributed globally via waves and pressure/temperature-gradient driven winds within hours (Burns et al. (1995), Mayr et al. (1984), and Prolss (1993)). There is thus a correlation between the rate of change in the semi-major axis of satellite orbits and geomagnetic activity, which can be visualized by observing an increase in spacecraft altitude decay during geomagnetic storms. Figure 1 shows this with the strongly positive correlation between the rate of de-orbit of 20 identical 3U satellites launched by Planet Labs, Inc. and geomagnetic activity represented by the strength of the Earth's ring current (Dst). These earth-observing 5 kg satellites are all sun-synchronous at altitudes in the vicinity of 450 km. The rate of change of altitude for these satellites was determined from two-line elements (TLEs), and averaged across all satellites in 6-hour windows. It was then compared to the 6-hour average of Kyoto Dst for the same time period, and shifted back in time by 6-hours to account for the delay in behavior between Dst and orbital decay (Figure 1a). This yielded a peak correlation coefficient of 0.76 (Figure 1b).

For the majority of small satellites deployed in the thermosphere, records of their semi-major axes are available in the form of TLEs, a data product provided to the public by the North American Aerospace Command (NORAD). They provide the mean orbital elements of a spacecraft at specific time, and are typically reported once a day for LEO spacecraft. The orbit determination method of Differential Correction (DC) is used to generate TLEs, and is essentially a multi-dimensional Newton-Raphson root solving method of $y = f(x)$ with a least-squares statistical treatment of the known data (y) provided by observations, either via GPS or visual/radar tracking (Vallado & Crawford, 2008). TLEs were designed to be used expressly for the purposes of orbit prediction with specific models, of which the most common is a set of Simplified General Perturbation (SGP) models referred to as SGP4 (Vallado et al., 2006). SGP4 is based off of theories of satellite motion described by Kozai (1959), Brouwer (1959), and Lyddane (1963), all of which neglected the effects of drag; SGP4 accounts for drag via power density functions (Hoots et al. (2004), Lane and Cranford (1969), Lane and Hoots (1979)) that require a term that encapsulates the ballistic coefficient, B^*, which can be used in the expression for the acceleration due to drag

$$a_D = \frac{\rho}{\rho_0} B^* \left(v - v_m\right)^2 = \frac{\rho B \left(v - v_m\right)^2}{2} = \frac{\rho C_D A \left(v - v_m\right)^2}{2m}, \tag{1}$$

where ρ is the local thermosphere density, ρ_0 is a reference air density given as 0.1570 $\mathrm{kg/m^2}/R_E$, B is the ballistic coefficient in units of area per mass, v is the velocity of the satellite, C_D is the drag coefficient, A is the cross-sectional area of the satellite as viewed from the ram direction, m is the mass of the satellite, and v_m is the velocity of the medium through which satellite is traveling. For LEO spacecraft, v_m is representative only of the rotation speed of the atmosphere, and usually neglects thermospheric winds. Unfortunately, the drag coefficient is often treated as constant. This fails to capture how the changing composition of the thermosphere with altitude affects the gas-surface interactions

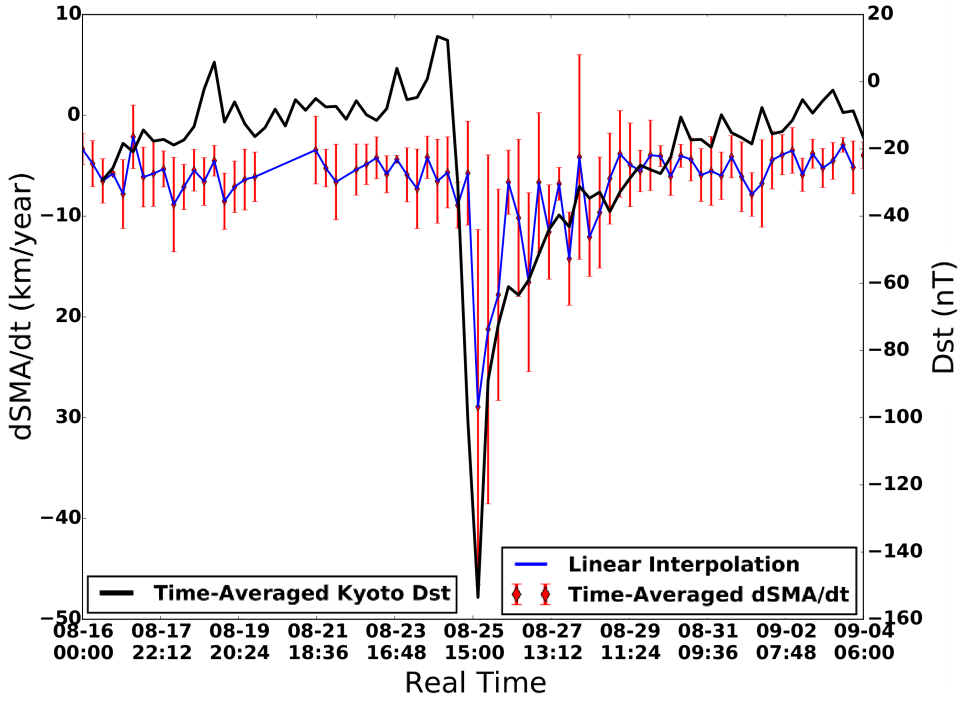

(a)

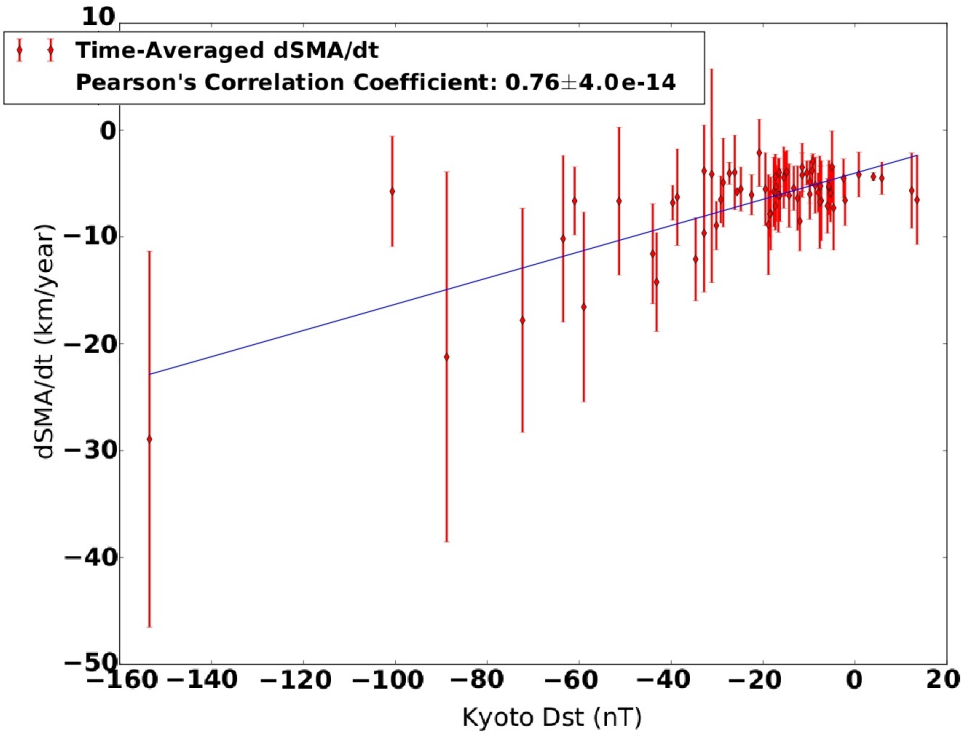

(b)

Figure 1: The rate of change of the semi-major of axis per year of 20 identical Flock 2K satellites overplotted with the Dst during a geomagnetic storm (top). Both the semi-major axis per year and the Dst have been averaged in six-hour time windows, and the value of the semi-major axis has been shifted forward in time by six hours to account for the characteristic time delay between initial storm onset and the resulting change in spacecraft altitude. Shown on the bottom is the positive correlation between the rate of change of the semi-major axis and of Dst for the same time period.

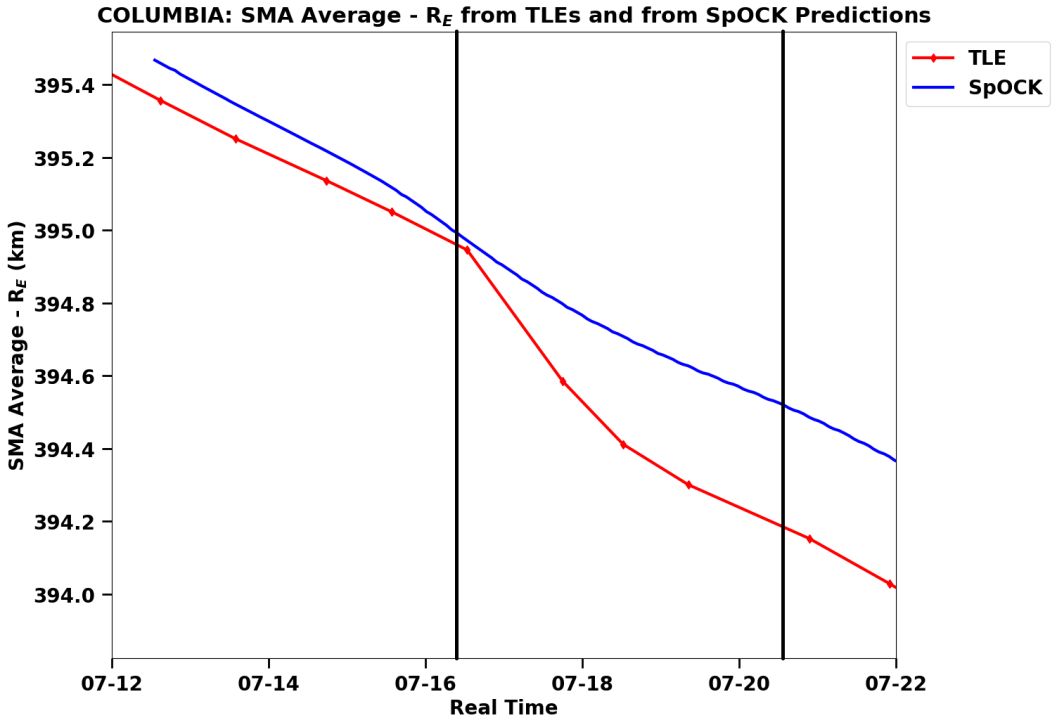

Figure 2: The orbital profile of the QB50 CubeSat Columbia superimposed with a reproduction of the orbit with SpOCK during a moderate geomagnetic disturbance that occurred between $\sim$ 3:00 UTC July 16 to $\sim$ 12:00 UTC July 20 of 2017 (black lines).

on the spacecraft faces, leading to a variable drag coefficient. The Spacecraft Orbital Characterization Kit (SpOCK), an orbital propagator developed at the University of Michigan, does not rely on B^* when using TLEs to perform orbit prediction. Instead, it allows the user to describe the spacecraft geometry with a CAD file or describe the orientation and area of all the spacecraft faces manually, and restricts itself to using the mean orbital elements from the TLE combined with an an accommodation coefficient (α) for the spacecraft surfaces, permitting the calculation of a variable drag coefficient (Bussy-Virat, Getchius, & Ridley, 2018). It currently relies on the NRLMSISE-00 empirical model for thermospheric density estimation.

Despite taking into account the drag, modeled altitudes, specifically during geomagnetic storms, under-predict the semi-major axis decline (Figure 2). Immediately after the storm onset, the spacecraft's rate of decay increases, but SpOCK, relying on MSISE for density estimation, fails to reproduce the deviation. These deviations are partially attributable to the limitations of empirical models, which rely on parametric fits to a catalog of density measurements taken from a variety of sources, including sounding rockets and accelerometer data from spacecraft (Picone et al., 2002). During quiet times, these models typically exhibit density errors on the order of 10% (Picone et al. (2002), S. L. Bruinsma et al. (2014)). These uncertainties increase greatly during geomagnetic storms for the reason that periods of intense geomagnetic activity are relatively infrequent and unpredictable, and their dynamical effects on the thermosphere are not understood well enough to provide for reliable density predictions over relatively short timescales. These limitations are exacerbated by biases in TLEs themselves; as the orbital elements encoded in TLEs constitute mean Brouwer-Lyddane elements, the process of their calculation smooths

out short-periodic affects in the elements that repeat on the order of a satellite's orbital period (Vallado et al., 2006).

This study presents a new technique that addresses the density uncertainty using TLEs from different satellites. The MSISE density inaccuracy can be probed by using SpOCK to reproduce satellite trajectories during both periods of quiet and active geomagnetic activity. As SpOCK relies on both MSISE and TLEs for initialization and propagation, estimation of calibration factors to the geomagnetic inputs to MSISE can yield a calibration method for thermospheric density models. A similar method has been shown to be successful by Doornbos et al. (2008), which involved the conversion of TLE data to drag data used in the daily adjustment of density model calibration parameters. This method found its inspiration in the Dynamics Calibration Atmosphere (DCA) used by the USAF's High-Altitude Satellite Drag Model (HASDM), which uses Space Surveillance Network observations of ∼75 orbiting spheres at various altitudes, performing a least squares differential correction across all satellites to solve for global density corrections to an empirical density model (Storz et al., 2005). While Doornbos et al. (2008) relied on the techniques in Picone et al. (2005) to calculate the density directly from individual TLEs before performing a least-squares adjustment to minimize the difference between TLE-derived densities and those of empirical models, we focus on minimizing the orbit error between altitude changes from SpOCK and those from TLEs, by estimating corrections to geomagnetic indices that are inputs to MSISE. This method, is referred to henceforth as the Multifaceted Optimization Algorithm (MOA). It is similar to the DCA used in HASDM, which simultaneously relates geomagnetic indices to the DCA correction parameters to the density and solves for a state vector for the calibration satellite. We perform corrections to MSISE densities during the May 2017 geomagnetic storm across ten identical 3U CubeSats of Planet Labs, Inc., and apply these corrections along the SWARM spacecrafts' orbits in order to directly compare the results with measurements.

Gondelach and Linares (2020) demonstrated the power of a Reduced-Order Model (ROM) that combines the predictive capabilities of physics-based models with the computational speed of empirical models in global density modeling. This technique is a full data assimilation scheme that is capable of using a variety of data sets, including accelerometer-derived densities, nonlinear space weather model inputs, modified equinoctial elements to describe satellite orbits, and TLEs. A dynamic model is derived that retains the primary characteristics of the state space describing the thermospheric density, but at lower dimensionality. In contrast to Gondelach and Linares (2020), the method described here demonstrates a simple way of improving density modeling that relies on less information and less processing. This method requires only spacecraft TLEs from a small number of objects, an orbital propagator, and geomagnetic indices, and demonstrates how improvements to storm-time density modeling can be achieved with limited information.

2 Methodology

2.1 Spacecraft Orbital Characterization Kit

SpOCK is an orbital propagator that simulates spacecraft location given a series of inputs that may either be entirely user-supplied or provided by various scientific databases. SpOCK is comprised of a suite of C functions that require the user to supply a geometry file and a main input file. The geometry file describes each face of the spacecraft, including the unit vector, the surface area, the total surface area of any solar cells on that surface, drag coefficient or accommodation coefficient, and the solar radiation coefficient. SpOCK requires specification of the solar irradiance, as proxied by F10.7. and the planetary activity level, as specified by 3-hour a_p. These are available through NASA OMNIWeb or NOAA's Space Weather Prediction Center (SWPC), and are used as inputs by NLRMSISE-00 to specify the thermospheric mass density. OMNIWeb gives static daily

F10.7, while SWPC gives a linear interpolation between daily values of F10.7. SpOCK's mathematical basis and capacity for parellelism is explored in detail in Bussy-Virat, Getchius, and Ridley (2018).

Once SpOCK is commanded to be run with the appropriate initialization information, it obtains an estimation of the local spacecraft density using MSISE. After calculating an estimate of the local drag and other perturbing forces, such as higher order gravity terms, gravity due to the Sun and Moon, solar pressure, and albedo effects from sunlight reflecting off of the Earth. SpOCK then propagates the trajectory of the spacecraft for a single timestep specified by the user in the main input file. SpOCK repeats this process until the given stopping point is reached. A large problem with techniques such as this is that the ballistic coefficient of the object is typically not known, unless the intent for the satellite is to derive the density. This is the case for satellites such as CHAMP, GRACE, and GOCE, as well as the reference spheres, but it is not true for many other objects. The ballistic coefficient can be derived from $B*$ in the TLE, but this is specifically designed for SGP4, so it is ignored. Instead, MOA uses a series of TLEs during quiet geomagnetic conditions to estimate the surface area of the object, assuming a mass and accommodation coefficient, from which a drag coefficient is derived.

2.2 Multifaceted Optimization Algorithm

MOA first collects TLEs for a specific satellite for a user-specified interval of time. It then uses the first TLE to initialize SpOCK and the subsequent TLEs in an attempt to reproduce the orbital profile by approximating the satellite geometry as a flat plate and using varying cross-sectional areas. MOA uses this basic framework in three processes that use TLEs from selected satellites to obtain corrected model densities (Figure 3).

The first process is the Area Optimization Algorithm (AROPT), which is a bilinear search algorithm that orbits a flat plate for a given time period, varying the area of the flat plate in each iteration, searching for the orbit trajectory that best matches the behavior of the altitude specified in the series of TLEs. AROPT first computes the orbit error for the upper boundary, then the lower boundary A_L, and finally the mean of both. These initial runs allow it decide between which values the optimized areas lies (Figure 4). The limits of the area search algorithm are twice the maximum expected projected area and half the minimum expected projected area. The real unknown for the orbit object is the ballistic coefficient, which is $\frac{C_D A}{m}$, but a mass and accommodation coefficient are approximated, implying that the real area and derived area may be different, depending on how far the C_D and mass estimates are off. The algorithm finds an area that allows the ballistic coefficient to minimize the error in the drag over the course of 2-3 days. This process assumes that the projected area is constant over the time period. This is most likely inaccurate, but it is permissible if the behavior of the object is repeating much faster than the minimization time period. For example, a tumbling object can be modeled with an average projected area, since it is most likely tumbling much more quickly than the optimization period. This assumption will fail if the object is systematically changing attitude for long periods of time. For example, the Cyclone Global Navigation Satellites (CYGNSS) satellites switch to a high drag mode for several days at a time to reduce the semi-major axis. This optimization scheme would work within the low-drag time and the high-drag time, but would not come up with a proper area during the transition. The sun-pointed satellites used in this study have areas that change through an orbit, but that change is rapid compared to the minimization time-period ($\sim$24 hrs), allowing an average area to be deduced. The accommodation coefficient was assumed to be 0.9 for all spacecraft surfaces. This was used to calculate a variable drag coefficient using Equations 2 and 3 from Moe et al. (2004). The mass of each satellite was assumed to be a constant 5 kg.

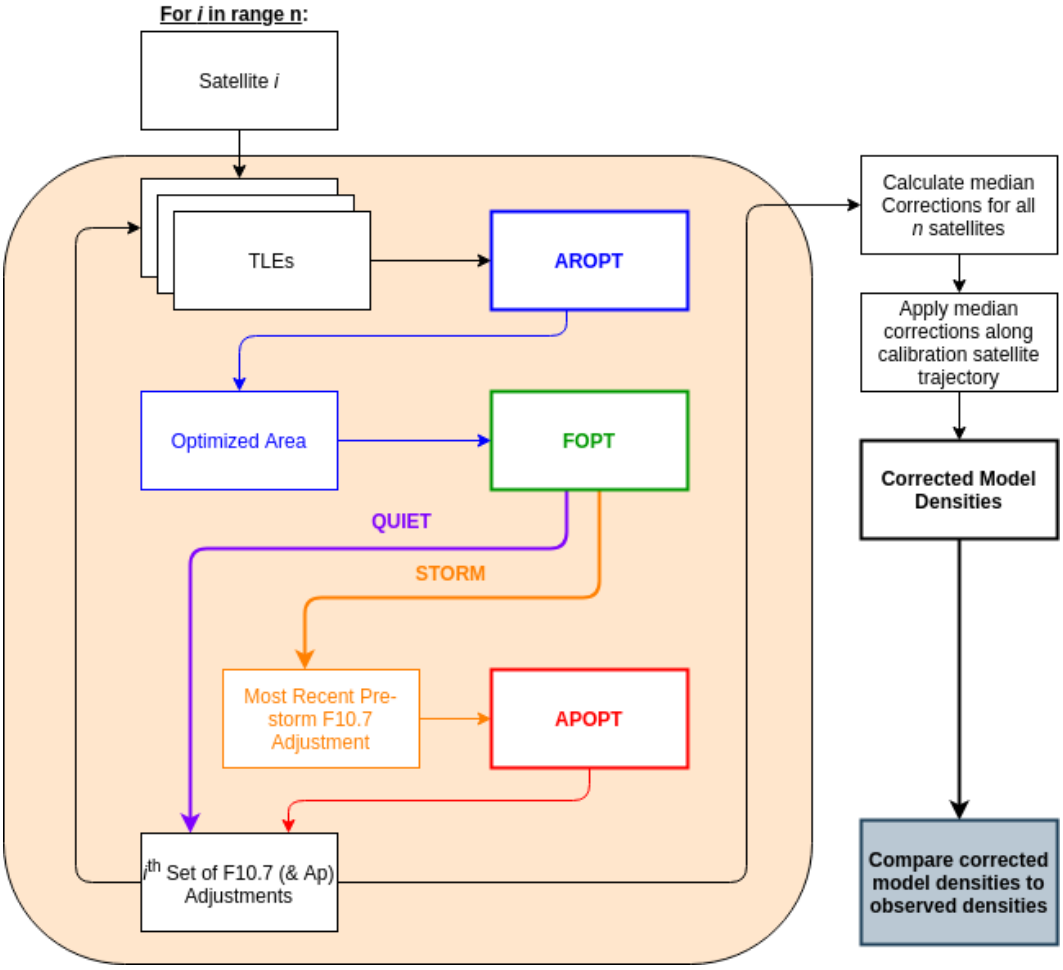

Figure 3: A flow-diagram of the Multifaceted Optimization Algorithm progressing from TLEs to corrected model densities.

A single run of AROPT is shown in Figure 5 for one of the 3U 'Flock 3P' satellites built by Planet Labs, Inc. The solid magenta line shows the altitude of the spacecraft as given by its TLEs, while the dashed lines show altitudes for the spacecraft simulated by SpOCK for different cross-sectional areas. The first three of those dashed lines indicate the lower, upper, and central boundaries used by AROPT, while the following 6 dashed lines are the results of AROPT running for different projected areas between the central and upper boundaries.

The same time period was run multiple times using a bilinear search algorithm until the error was less than 1 m. This general search for the optimum area typically took around six iterations. The area optimization was conducted for subsequent intervals of time, creating a time series of optimized areas. After the completion of these runs, a histogram of the optimized areas was generated, along with a graph showing the behavior of the optimized areas over the entire period. A histogram of optimized areas for this spacecraft over an 15-day period is shown in Figure 6, where the dashed magenta line represents the 50th-percentile optimized area found by AROPT.

Using AROPT as the first step in MOA allows an inference of the orientation of the chosen spacecraft. For a spacecraft with known geometry, comparing the optimized

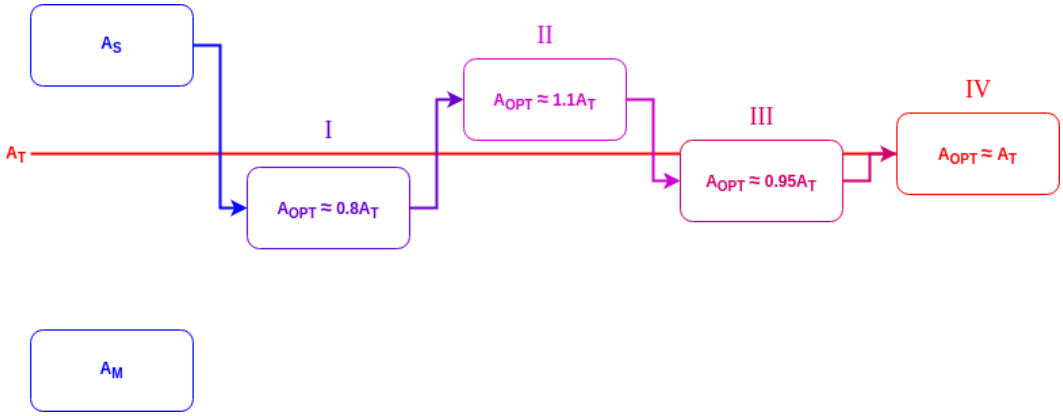

Figure 4: The behavior of the AROPT for a scenario where the true optimized area A_T (red line) is between the upper boundary A_S and the mean of the lower and upper boundaries A_M. Only 4 cycles are shown in this schematic. Typically, AROPT took at least 6 iterations to converge (resulting in an semi-major axis error $\leq 10^{-3}$ km).

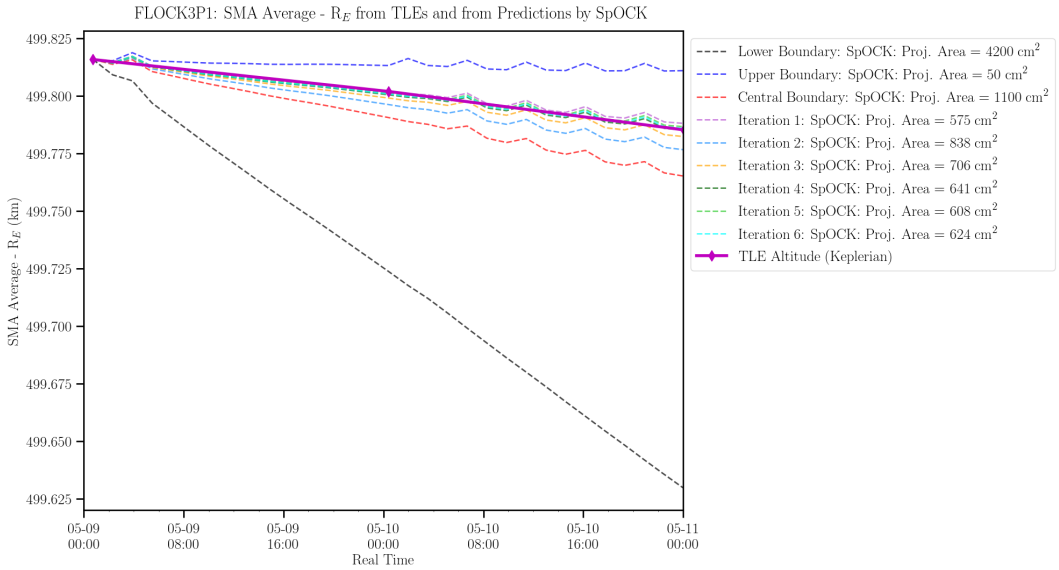

Figure 5: An example of a completed AROPT run for the FLOCK 3P 1 3U CubeSat. The top three lines in the legend correspond to the creation of the lower boundary (twice the largest face of the spacecraft), upper boundary (half the smallest face of the spacecraft), and the middle cut (the mean of the largest and smallest faces). The last iteration in the legend corresponds to the optimized area found after all of the cycles. 'TLE Altitude' refers to the altitude derived from the semi-major axis computed from the TLEs for the spacecraft.

areas returned by AROPT to the projected areas of the spacecraft from each of its sides allows us to get an idea which side of spacecraft is likely pointing towards the direction of travel. AROPT therefore represents a method of accounting for spacecraft variable geometry (deployable panels and antennae), and changes in attitude. AROPT selected a specified percentile from the distribution function of areas as the constant area to be used by the remaining sub-process(es) (e.g., in Figure 6 the median value of 640.63 cm^2).

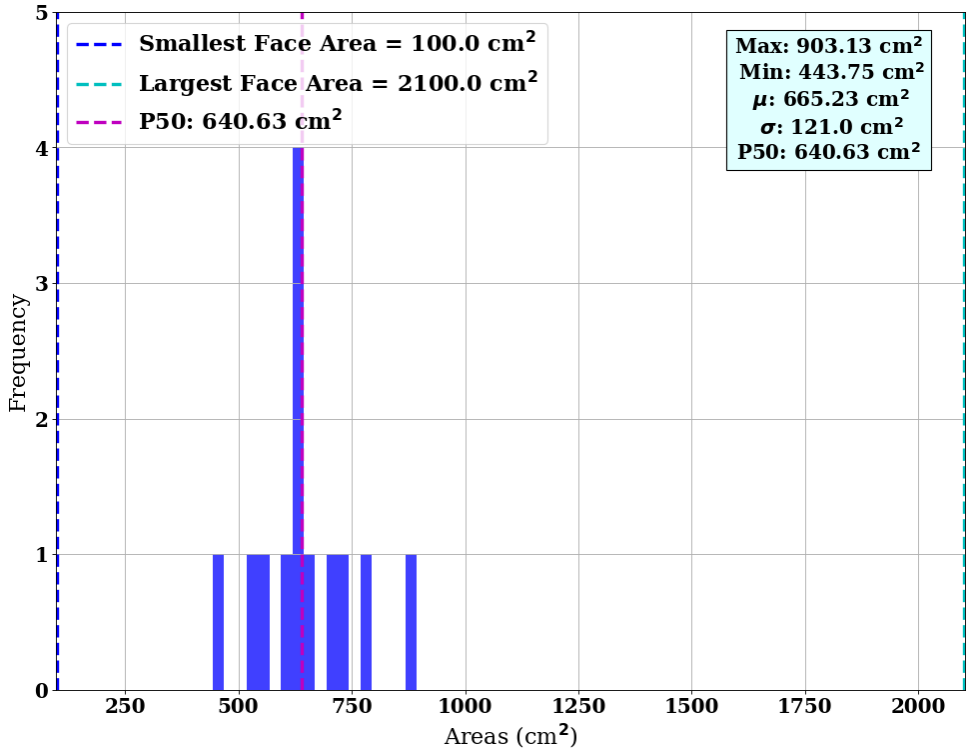

Figure 6: A histogram of optimized areas found by AROPT for the FLOCK 3P 1 spacecraft between 2017-05-09 and 2017-05-24.

The rationale behind the selection of a specific quartile assumes the rate of de-orbit of the satellite in question will be overwhelmingly attributable to changes in the space environment captured by the behavior of geomagnetic indices. The optimized areas found by AROPT will be inextricably tied to the empirical model from which SpOCK receives an estimate of the density, as the finding of these areas essentially compensate for bias in the model. The optimized area obtained by AROPT will add bias in the downstream predictions, since it will be the static area for the F10.7 and 3-hour a_p optimization. The goal of the area optimization is to allow a static area to be chosen, so that the thermospheric density can be altered away from the NRLMSISE-00 predicted values. This assumes that, on average, during the two-week quiet interval selected for the area optimization, NLRMSISE-00 predicted the correct mass density, but the values at time-scales smaller than a couple of weeks may incorrect. It is emphasized that variation in area (Figure 6) could be due to (1) discrepancies between NLRMSISE-00 and reality; (2) errors in TLEs; or (3) issues with F10.7 and a_p describing the thermosphere during the optimization interval. This technique assumes that, on average MSISE, the TLEs, and the models used to generate F10.7 and a_p are unbiased such that the average of each of the those errors over a long time (over the ∼week-long period being considered) cancels.

Once a ballistic coefficient for an object is derived, the thermospheric density corrections can be derived. This is done across two time scales with two different indices- namely the F10.7 to represent ∼24-hour density corrections and a_p to represent 3-hour density corrections. By altering these indices, the global density can be altered, as opposed to the localized density. These alterations on the indices don't imply that the indices themselves are incorrect, but are a way to alter the NRLMSISE-00 densities without actually altering the NRLMSISE-00 source code, or using an arbitrary multiplica-

tive factor. The FOPT and APOPT processes are bilinear search algorithms like AROPT, except they alter F10.7 and 3-hour a_p, respectively. In order to set upper and lower boundaries, however, FOPT and APOPT set limitations to maximum and minimum values of F10.7 (200 sfu and 80% of the value of the smallest F10.7 value in the interval, respectively) and 3-hour a_p (400 and 0, respectively), and subsequently bracket between those limits to find the correction necessary to minimize orbit error. APOPT and FOPT do not apply corrections to the geomagnetic indices in a multiplicative manner, but in an additive manner. The FOPT process is run after AROPT is complete.

APOPT only runs if MOA determines that a geomagnetic storm has occurred during the specified interval. It does this using data from the World Data Center for Geomagnetism, and considers any geomagnetic disturbance in which Dst passes below -50 nT to be a storm (Akasofu, 2018). In such a case it will run APOPT for the two days following the date of initial storm onset, in order to account for the duration over which the impact of geomagnetic activity is felt globally. APOPT runs while holding the most recent correction to F10.7 obtained via FOPT constant throughout the duration of the storm. This is done for the reason that F10.7 not only varies on much longer timescales on the order of days (see Figures 11 and 12 in Wang et al. (2018)) than 3-hour a_p which varies on the order of hours (see Figure 1 in Wrenn (1987)), but it also is only collected once a day. Therefore, any rapid changes in the density during stormtime will most strongly correlate with fluctuations in 3-hour a_p, and almost not at all with F10.7. Base values of F10.7 and a_p data are either taken from NASA's Space Physics Data Facility OMNIWeb service or SWPC. This data source selection is held constant throughout all of the sub-processes.

Across all three processes, orbit error minimization is performed using the root mean square error (RMSE). The RMSE (δ_z) between SpOCK altitude values (ξ_i) and the corresponding timesteps closest to those of the TLE altitudes in the interval of the run (i=0:T) in question is calculated:

$$\delta_z = \sqrt{\frac{\sum_{i=0}^{N} \left(\xi_i - h_i\right)^2}{N}}, \tag{2}$$

where N is the number of TLEs within the optimization interval. This method minimizes the RMSE between the SpOCK altitudes and TLE altitudes throughout the entire profile within the interval, using a bilinear search algorithm. This difference provides a more relevant comparison as opposed to differencing the ending altitude.

3 Results

In order to demonstrate the MOA technique, the time period of May 23, 2017 - June 6, 2017 was explored and is presented here. During this time, ten Flock 3P spacecraft (Figure 7) launched by Planet Labs, Inc. were on orbit (Table 1, Figure 8), and a geomagnetic storm of moderate strength took place (Figure 9). The FLOCK 3P were in sun-synchronous orbits between 490-500 km in altitude. Multiple satellites were used to optimize the density corrections, which were then compared to accelerometer-derived densities from the SWARM spacecrafts.

The same geometry file was used for each of these satellites: all of the CubeSats of the 'Flock' series launched by Planet Labs, Inc. are identical and can be described as ordinary 3U CubeSats with deployed solar panels normal to the zenith direction possessing an area of approximately 1200 cm^2. The mass of each spacecraft was fixed at 5 kg. As they were earth-imaging and sun-synchronous, their solar panels were always angled towards the sun, and as a result the projected cross-sectional area was expected to vary around 1000 cm^2.

Name	NORAD ID	P25 (cm^2)	P50 (cm^2)	P75 (cm^2)	σ (cm^2)
Flock 3P-1	41967	611.91	640.63	730.86	121.00
Flock 3P-2	41966	517.58	755.47	964.65	288.80
Flock 3P-3	41968	804.69	837.50	1034.38	146.35
Flock 3P-4	41965	640.63	812.89	899.02	207.67
Flock 3P-5	41971	484.77	804.69	870.31	292.81
Flock 3P-6	41969	858.00	927.73	1100.00	129.80
Flock 3P-7	41970	702.15	894.92	1095.90	196.25
Flock 3P-8	41951	706.25	829.30	972.85	234.95
Flock 3P-9	41973	714.45	1050.78	1100.00	231.64
Flock 3P-10	41974	616.02	927.73	1087.70	242.73
Mean	-	665.65	848.16	985.57	209.2

Table 1: The 10 Flock 3P satellites for which TLEs were collected for the run between 2017-05-23 and 2017-06-02. The 25th, 50th, and 75th percentile areas with standard deviations from the optimized area distributions found for each satellite by AROPT are found in the right three columns.

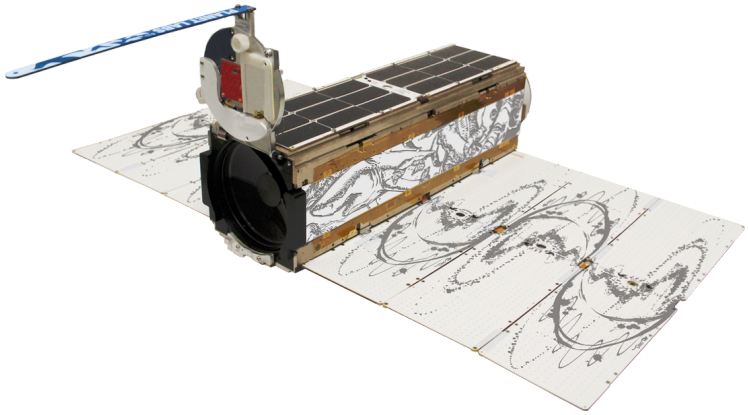

Figure 7: An image of one of the Flock 3P satellites (Source: Spaceflight101; used with permission from Planet Labs, Inc.).

As described above, F10.7 corrections are strongly influenced by the percentile of the optimized area distribution chosen. The corrections to F10.7 in and of themselves are merely a means of correcting the density, and are not the object of this study. We elected to compute corrections using the 25th, 50th, and 75th percentiles of the optimized area distribution in order to determine its effect on the adjusted densities. For each of the 10 satellites, the following procedure was conducted:

- The area distribution function was determined over the selected time period.
- F10.7 corrections were then calculated over that interval.
- 3-hour a_p corrections were finally calculated during the main phase of the storm.

Once this was completed, median daily F10.7 values were generated using results from all 10 satellites. These medians were calculated from constant F10.7 corrections in each 24-hour interval, and associated with noon of their respective days. Finally, median 3-hour a_p corrections were generated during the storm main phase, and associated with

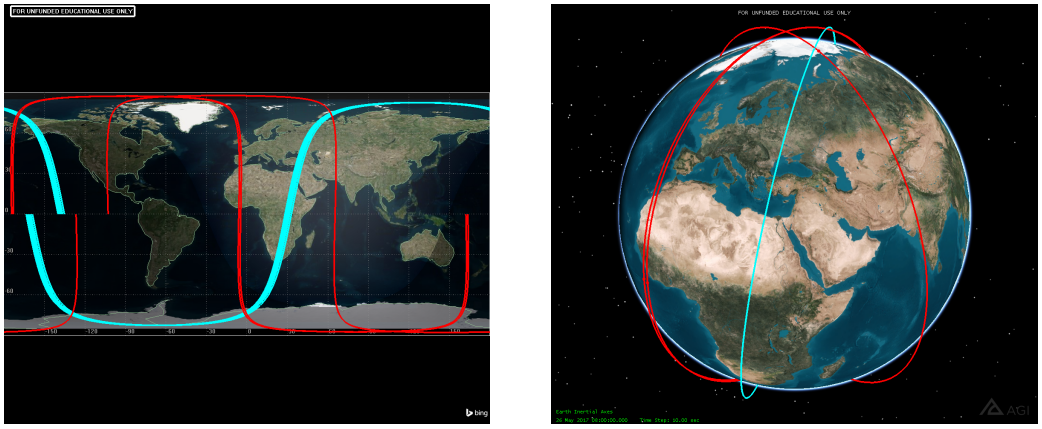

(a) (b)

Figure 8: Visualizations of the ground tracks of the Flock 3P constellation and SWARM spacecraft in Satellite Tool Kit - Analytical Graphics, Inc. (left). The same orbits shown for a globe (right). The orbits of the Flock 3P satellites are in cyan, and those of the SWARM spacecrafts are in red.

the zeroth hour of their respective days, as this resulted in more accurate corrected storm-time densities than when the corrections were associated with noon of their respective days. To validate the efficacy of the method, MSISE was run at the locations of the three SWARM satellites using the modified median F10.7 and a_p values. We focus on three major metrics to perform validation:

1. $\boldsymbol{\delta_P}$: Percent difference between the peak orbit-averaged density between uncorrected NRLMSISE-00 orbit-averaged densities, MOA orbit-averaged corrected densities and orbit-averaged SWARM accelerometer data:

$$\delta_P = \frac{|\rho_N - \rho_S|}{\left[\frac{\rho_N + \rho_S}{2}\right]} \times 100\% \tag{3}$$

   where ρ_N is either the NRLMSISE-00 or MOA orbit-averaged density and ρ_S is the SWARM accelerometer-derived orbit-averaged density.
2. $\boldsymbol{\eta}$: Ratio of the peak orbit-averaged density magnitude to the 24-hour averaged orbit-averaged density prior to the peak density within the 24 hours immediately preceding the peak density.
3. $\boldsymbol{\rho_T}$: Total time-integrated density in $\frac{\text{kg}\cdot\text{s}}{\text{km}^3}$ during the main phase of the storm. In order to set the boundaries for calculating this integral, the following was done: (a) For each point, the arithmetic mean density and standard deviation of the density for the SWARM orbit-averaged density for the preceding 12 hours. (b) The lower bound of the integral is found where both the density exceeds the mean + standard deviation at its associated time, and when all of the density values for the next 12 hours satisfy that condition. (c) The upper bound of the integral is found using the same method, but going backwards from the density values at the end of the chosen time period.
4. $\boldsymbol{t_l}$: The time difference in hours between the peak in the NLRMSISE-00 or MOA orbit-averaged densities and the peak in the SWARM accelerometer-derived orbit-averaged densities.

The two SWARM spacecraft chosen allow us to determine the utility of our corrections to global geomagnetic indices along orbits at different altitudes. The SWARM-

A spacecraft orbits at an altitude of ∼460 km and inclination of 87.4°. SWARM-B orbits higher at ∼530 km in altitude and an inclination of 88°.

3.1 Optimized Areas and Corrections to F10.7 and 3-hour a_p

The geomagnetic indices during and surrounding the May 27-28, 2017 storm are shown in Figure 9a. During this time 3-hour a_p surged sharply, peaking at ∼ 130 nT on May 28th, while Dst reached a minimum of -125 nT. This increase a_p was associated with the density change that perturbed the orbits of the spacecraft, and affected the baseline densities on which corrections were performed. F10.7, in comparison, exhibited negligible variation.

The rate of change of the Flock 3P satellites' semi-major axis derived from the TLEs are shown in Figure 9c. A clear increase between May 28 and May 30 corresponded to the main phase of the storm. The average maximum rate of change attained by the constellation during the storm main phase was over 20 km/year. This maximum occurred between May 29th and May 30th, even though the storm's peak intensity, as indicated by 3-hour a_p, occurred on the 28th. This delay in behavior is likely due both to the lower time resolution of TLEs, and the fact that changes in the local density outside of high latitudes do not occur immediately in response to geomagnetic activity, but often hours later (Oliveira et al. (2017), Guo et al. (2010)). There is a slight drop in the rate of change of the semi-major axis (dSMA) around May 26th just prior to the main phase of the storm. This drop is also observable in of all of the Flock 3P satellites, which may suggest a persistent structure in the thermospheric density response that has a consistent effect on all of the satellites. This indicates that the thermospheric density was most likely lower than expected on this day. It should be understood that the change in SMA is due to the integral of the density in the time prior to the measurement. These changes do not directly reflect changes in the instantaneous density.

The optimized area distributions found for each satellite clustered around 800 cm^2 (Figure 10.) If 0° is considered to be parallel with the direction of travel, these results suggest that the Flock 3P satellites' largest face consisting of the solar panels was at an orbit-averaged angle of ∼20°. The high degree of overlap of the distributions suggests the orientations of the spacecraft were very similar during the time period. The notable exception was Flock 3P 1, which may have either have had its solar panels slightly closer to parallel, or may have had panels that incompletely deployed, as suggested by its high count of values around 600 cm^2.

Subsequently-derived F10.7 corrections corresponding to each percentile of the optimized areas all exhibit a drop around May 26th before they peaked during the main phase of the storm (Figures 11 and 12), similar to the behavior of the dSMA. They all consistently declined during the recovery phase. This pre-storm drop may have been due to FOPT responding to the peak in F10.7 on the 27th, which occurred just over a day before the peak intensity of the storm on the 28th. This is clearest in Figure 13, where the peak negative F10.7 corrections preceded the peak uncorrected F10.7 values by one day. There was a general trend of the F10.7 corrections becoming less positive as a function of increasing percentile, while the overall behavior was preserved. The closeness of the lines corresponding to the 50th and 75th percentile suggest that this behavior tapered as the percentile increases. This is shown by the smaller mean difference between the 75th percentile areas and 50th percentile areas (∼ 137.40 cm^2), compared with the 50th percentile areas and the 25th percentile areas (∼ 182.51 cm^2). As the cross-sectional area increased, the drag became an increasingly larger force, resulting in MOA lessening the contribution of increased F10.7 to compensate for the increase.

Similar to the F10.7 corrections, MOA's a_p corrections exhibit an increase beginning on or before May 28th, but this increase was much sharper, as the corrections jump from -5 nT on the 28th to +80 nT on the 29th. This kept the 3-hour a_p to NRLMSISE-

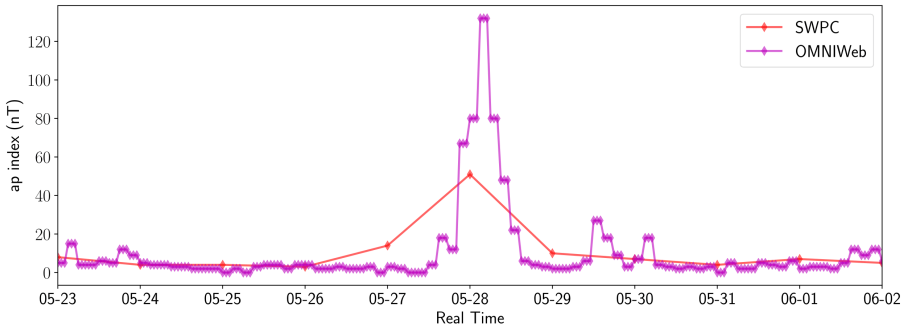

(a)

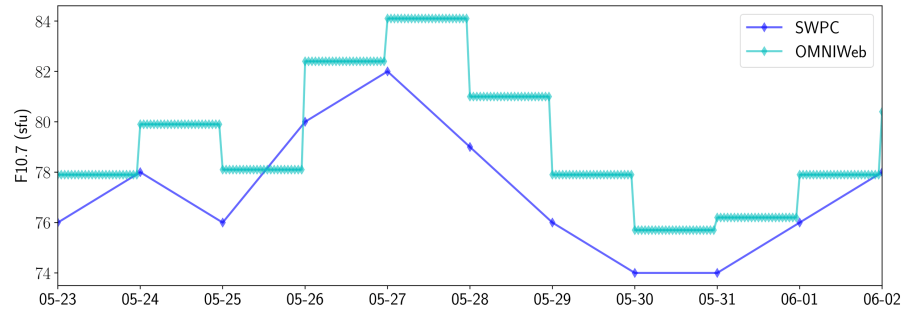

(b)

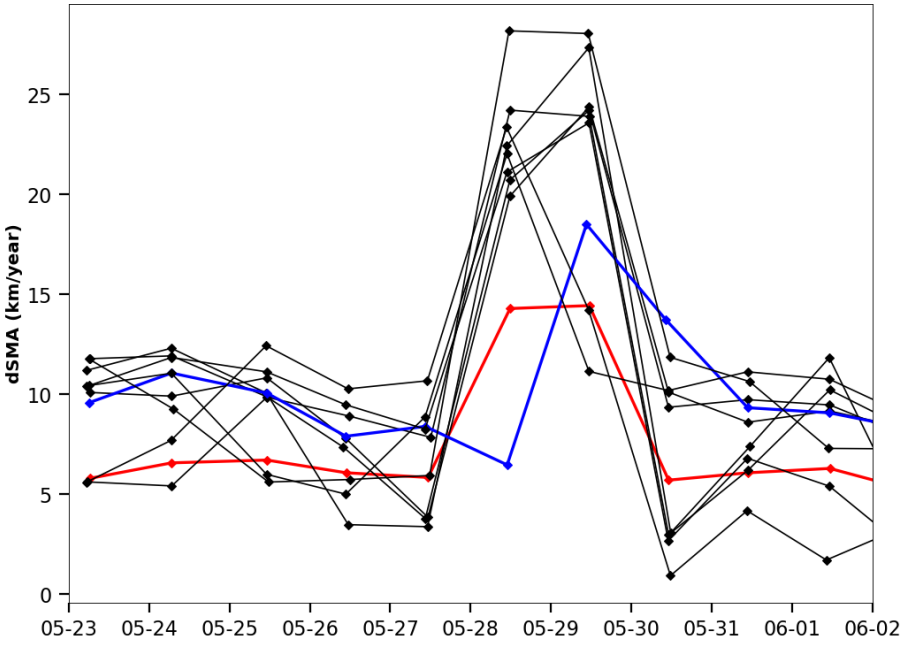

(c)

Figure 9: Geomagnetic indices provided by NASA OMNIWeb and NOAA SWPC during the geomagnetic storm of May 2017 ((a) and (b)). TLE-derived rate of change of the semi-major axis for the Flock 3P satellites (c). The rates of change for Flock 3P-1 (red) and Flock 3P-6 (blue) display unique behavior.

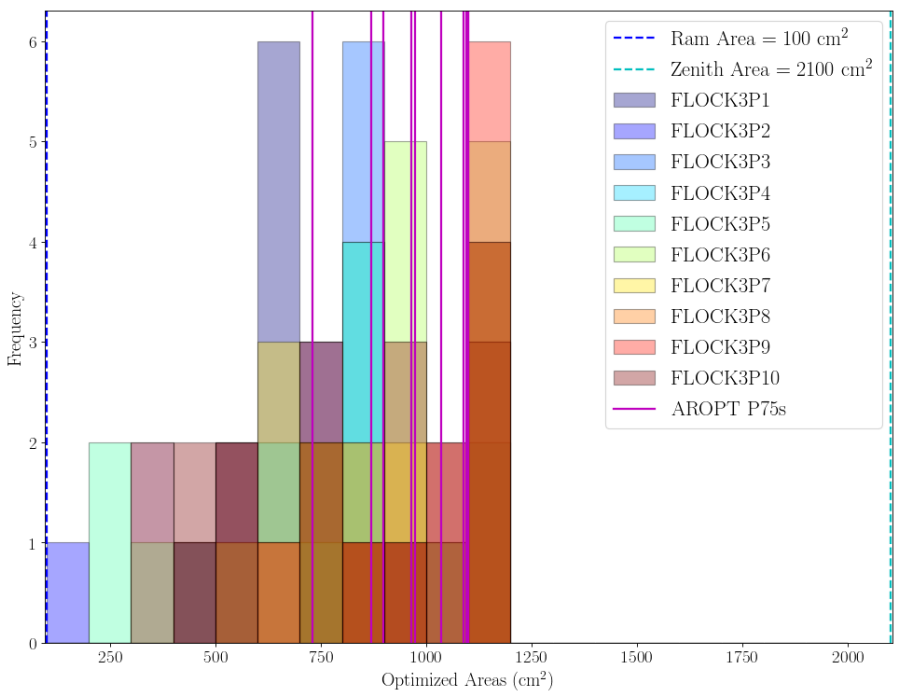

Figure 10: Overlapping histograms of the optimized area distributions for each Flock 3P satellite. The vertical magenta lines are the 75th percentiles of each distribution.

00 much higher after they reached their peak value of $\sim$ 140 nT on the 28th, before dropping sharply immediately after the start of the 29th.

MOA's F10.7 and a_p corrections were used to drive the perturbations needed to get NLRMSISE-00 to provide the best density predictions. The linearly-interpolated median corrections were applied to F10.7 inputs to NLRMSISE-00 during the initial and recovery phases of the storm and to the a_p inputs to NLRMSISE-00 during the main phase of the storm, resulting in corrected densities along that satellite's orbit. The strength of this technique lies in that it derives corrections to global drivers for NLRMSISE-00, allowing a specification of the density at any other location in the thermosphere. This can be used not only to derive better densities for orbit propagation for other satellites, but also to specify model biases for prediction.

3.2 SWARM Density Comparisons

In order to validate the technique, the NLRMSISE-00 mass densities along the SWARM satellite orbit tracks were calculated using the unperturbed drivers and the MOA-derived perturbed drivers. We first consider the effects of the selection of the quartile of the optimized area on the resulting orbit-averaged corrected densities along the trajectories of each SWARM spacecraft. This de-biases the predicted drivers, since the absolute area is unknown. With enough data-model comparisons, an appropriate quartile can be selected and used for all future simulations. Figure 14 shows a comparison between SWARM-derived and MOA-derived densities with different quartiles of the area selected. The average altitudes of SWARM-A and SWARM-B during the time chosen were $\sim$ 452 km

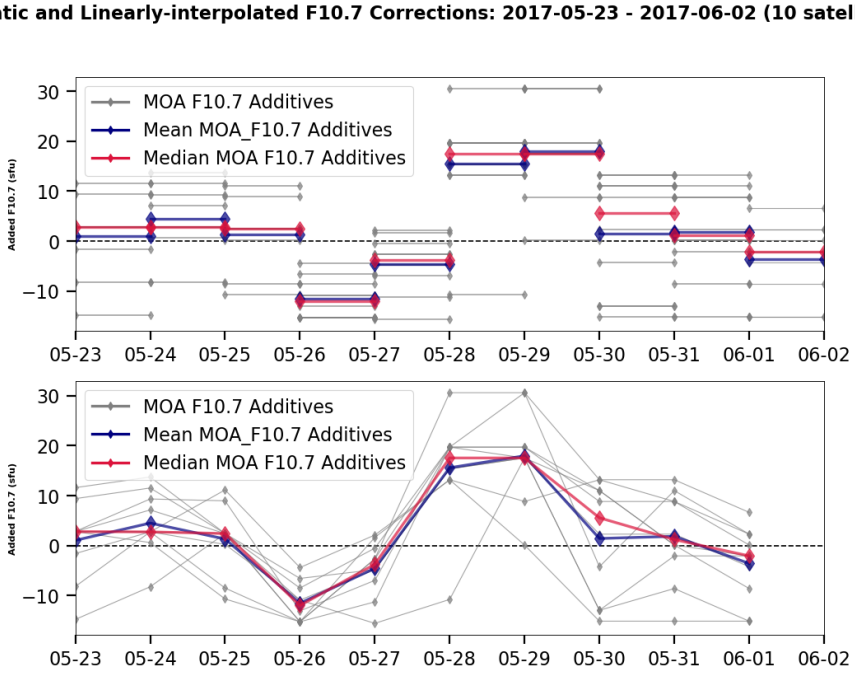

Figure 11: Static (top) and linearly-interpolated (bottom) F10.7 corrections obtained for the 75th-percentile optimized area. The static corrections are applied for two days during the optimization interval, but are shown as lasting for one-day in the top plot in order to declutter the figure. The mean corrections obtained across each optimization interval are in blue, and their median counterparts are in red.

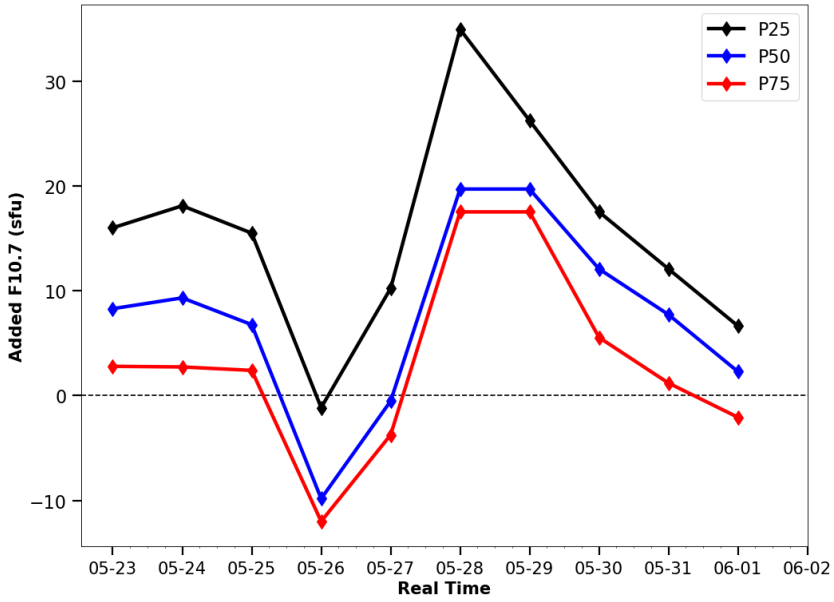

Figure 12: Linearly-interpolated median F10.7 corrections corresponding to the MOA runs where the 25th (black), 50th (blue), and 75th (red) percentiles were used. These results were from runs driven by OMNIWeb inputs.

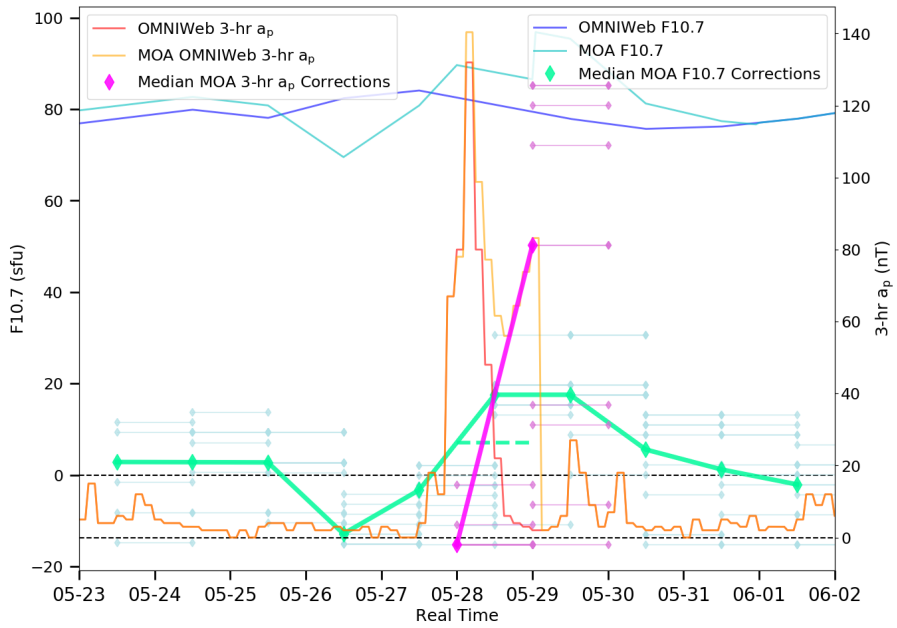

Figure 13: An overlay of the uncorrected F10.7 OMNIWeb values (purple), MOA's corrected F10.7 values (cyan), MOA's F10.7 median corrections corresponding to the 75th percentile (green), and the individual corrections across each satellite (dimmed green), and uncorrected OMNIWeb 3-hour a_p values (orange), MOA's corrected 3-hour a_p values (light orange), MOA's 3-hour a_p median corrections to the 75th percentile (fuchsia) and the corresponding individual corrections across each satellite (dimmed fuchsia). Note the dashed green line showing the value of the F10.7 corrections held constant during the application of 3-hour a_p corrections.

and $\sim$ 515 km, respectively. From those, we derived a time resolution for the orbit-averaged densities of $\sim$ 93.6 minutes and $\sim$ 94.9 minutes for each satellite, respectively.

SWARM-A Orbit-Averaged Density Metrics					
Source	maxρ $\left(\frac{\text{kg}}{\text{km}^3}\right)$	δ_P	t_l (hours)	η	ρ_T $\left(\frac{\text{kg·s}}{\text{km}^3}\right)$
SWARM	7.8×10^{-4}	-	-	2.6	98.3
NLRMSISE-00	6.6×10^{-4}	17.6	4.7	2.9	79.8
MOA	7.3×10^{-4}	7.5	4.7	3.2	101.1

Table 2: Tabulated values of the peak orbit-averaged density maxρ, δ_P, t_l η and ρ_T along SWARM-A.

During the main phase, the peak orbit-averaged densities returned by each MOA's percentiles were very close to the peak orbit-average densities for SWARM, with the 50th and 75th percentile cases being closest together. Along SWARM-A, percent errors between peak orbit-averaged MOA densities and those from SWARM were $\sim$2.4%, $\sim$5.9%, and $\sim$7.7%, for the 25th, 50th, and 75th-percentile optimized areas, respectively (Fig-

ure 14a). Note that increasing the percentile of the optimized area slightly reduced the accuracy in the peak orbit-averaged density along SWARM-A.

Along SWARM-B, this trend was reversed, with the 25th-percentile case yielding a peak orbit-averaged density error of ∼19.1% compared to ∼10.4% and ∼8.6% for the 50th-percentile and 75th-percentile cases, respectively (Figure 14b). The rest of this study only considers the 75th-percentile case.

As shown in Table 2, usage of MOA's corrections along SWARM-A resulted in a max ρ, δ_P, and ρ_T all closer to those of the SWARM data, compared to uncorrected MSISE. The closeness of ρ_T in particular demonstrates that MOA greatly improved the width of the peak density during the main phase of the storm. Table 3 confirms these improvements along SWARM-B to a slightly greater degree, with the exception of max ρ, which MOA overestimated by 8.61%. The difference in ρ_T along SWARM-A between MSISE and SWARM was 3% but this dropped slightly to 2.6% along SWARM-B.

SWARM-B Orbit-Averaged Density Metrics					
Source	maxρ $\left(\frac{\text{kg}}{\text{km}^3}\right)$	δ_P	t_l (hours)	η	ρ_T $\left(\frac{\text{kg}\cdot\text{s}}{\text{km}^3}\right)$
SWARM	2.9×10^{-4}	-	-	2.5	16.6
NLRMSISE-00	2.8×10^{-4}	4.6	4.6	3.8	11.7
MOA	3.2×10^{-4}	8.6	4.6	4.3	16.2

Table 3: Tabulated values of the peak orbit-averaged density maxρ, δ_P, t_l, η and ρ_T along SWARM-B.

Figure 15 overlays orbit-averaged densities from MSISE, MOA, and accelerometer data along SWARM-A and SWARM-B. It shows that the error in orbit-averaged density is reduced for MOA compared to uncorrected MSISE along SWARM-B, but not SWARM-A, though the values of ρ_T for MOA showed improvement over MSISE along both orbits. Along SWARM-A, the percent error between MOA ρ_T and SWARM ρ_T was $\sim 2.9\%$, compared to a percent error of $\sim 23.6\%$ for MSISE. Along SWARM-B, the percent error between MOA and SWARM was slightly lower, at only $\sim 2.7\%$, compared to $\sim 34.8\%$ for MSISE. Visually, this translated to a widening of the peak in the orbit-averaged density. This behavior can be observed in Figure 15, where MOA orbit-averaged densities between 05-28 and 05-29 were noticeably higher than their uncorrected NLRMSISE-00 counterparts. MOA matches SWARM quite well during the recovery of the storm, showing the same drop-off in density around the 29th. Along SWARM-A and SWARM-B, MOA attempted to recreate the second peak in the density occurring just before the 29th, but was unable to reach the necessary amplitude to do so to the most accurately degree possible. This is especially obvious along SWARM-B. Finally, along both SWARM spacecraft, MOA placed the time of the peak orbit-averaged density as identical to that of MSISE. The times of the peak density, as shown in Tables 2 and 3 were an average of 4.7 hours prior to that of the SWARM data. This may be due to the fact that MSISE and MOA are unable to account for the time delay between when geomagnetic indices peak and when local density at the spacecraft peaks. MSISE and MOA apply geomagnetic indices instantaneously, which fails to capture this delay, which according to the literature, can be up to 4 hours in duration (S. L. Bruinsma et al., 2006).

Outside of the main phase, where only the corrections to F10.7 were applied, MOA performed marginally better than NLRMSISE-00 just before initial storm onset along SWARM-A, and just after the recovery phase along SWARM-B. Both NRLMSISE-00

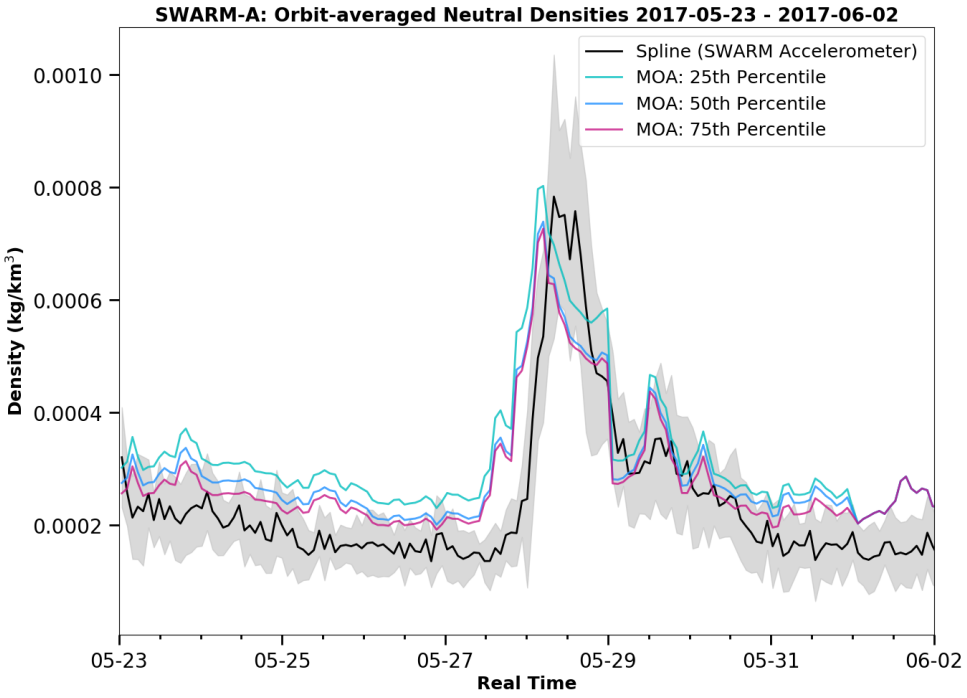

(a)

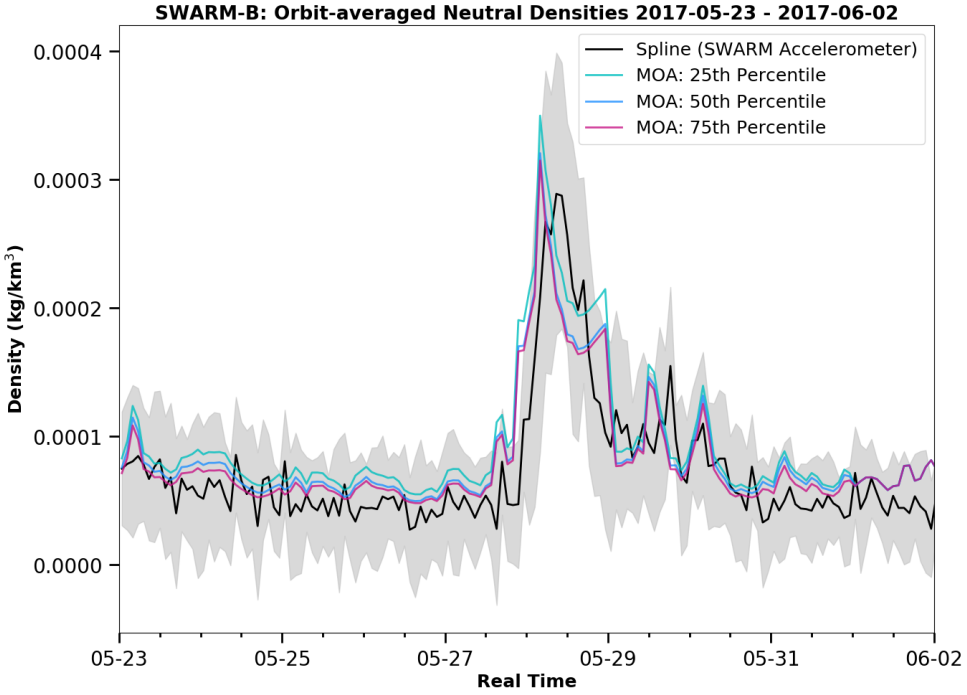

(b)

Figure 14: Orbit-averaged densities along-track SWARM-A (a) and SWARM-B (b) and for OMNIWeb inputs, with results shown corresponding to the percentiles of the optimized area. The gray area around the SWARM orbit-averaged densities denotes the $\pm 1\sigma$ boundaries.

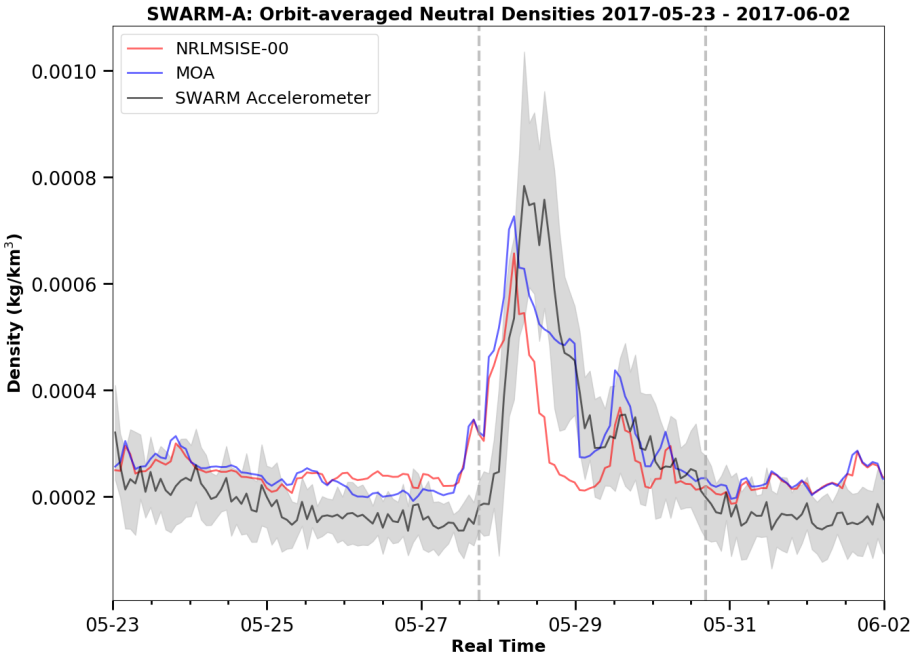

(a)

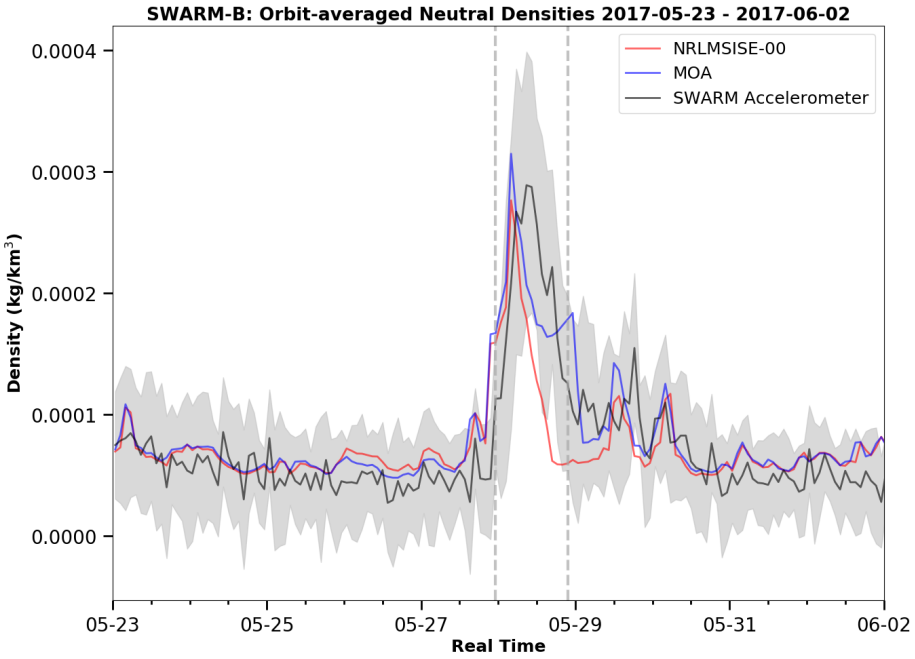

(b)

Figure 15: Orbit-averaged densities along-track SWARM-A (a) and SWARM-B (b) for OMNIWeb inputs. MOA results corresponding to the 75th-percentiles are in cyan, uncorrected MSISE results are show in red, and SWARM data is shown in black. The gray vertical dashed lines represent the boundaries of the integral used to calculate ρ_T across each dataset, and the gray area around the SWARM orbit-averaged densities denotes the $\pm 1\sigma$ boundaries.

and MOA overestimated the density during the initial and recovery phases along SWARM-A, though in the former case, MOA did so to a lesser degree, especially along SWARM-A. Along SWARM-B, the overestimation before the initial phase and after the recovery phase was much less noticeable, with MOA and MSISE densities all residing within the 1σ boundaries of the SWARM densities. The corrections to F10.7 were rather marginal compared to 3-hour a_p, and never exceeded $\sim |17|$ sfu, compared to 3-hour a_p corrections, which grew to a maximum of +80 nT on the 29th.

4 Discussion and Conclusion

While widespread use of empirical density models like those of the MSISE family are a testament to their efficacy and utility, this study highlights some of their limitations during high levels of geomagnetic activity. These limitations are in part largely owed to the expected biases characteristic for any model. Algorithms like HASDM Storz et al. (2005), circumvent this problem by relating corrections in the density to estimated scale factors to temperature, F10.7, and a_p. As biases are to be found in any model, the usage of correction factors to account for them is expected, and it is only a matter of how they are to be derived, and how they are to be applied. From the close correspondence between orbit-averaged densities returned by MOA and *in-situ* data collected by the SWARM spacecrafts, this preliminary study suggests that TLEs can be used effectively to correct empirical model densities through the process of orbit-error minimization in a relatively simple process. Doornbos et al. (2008) used a similar method, but their method differs from MOA in that it directly derived densities from TLEs in accordance with the methods in Picone et al. (2005), and used a least-squares adjustment to estimate a set of calibration parameters to height-dependent scale factors of the densities and CIRA-72 temperatures. MOA does not rely on TLE-derived densities themselves to perform calibration, but rather relies on TLE-derived semi-major axes, and retrieves a corrected density by determining corrections to NLRMSISE-00 drivers to match those variations in semi-major axis. Gondelach and Linares (2020) also presented a powerful method for both modeling storm time densities and performing density prediction by assimilating TLEs and historical empirical model density estimations into a reduced-order model (ROM), that allows for very accurate real-time density prediction. MOA differs from the ROM in that it is simple to implement, not requiring the estimation of ballistic coefficients with the use of a Kalman Filter, the modification of equinoctial elements, or the assimilation of accelerometer data from multiple sources. Additionally, MOA demonstrates the capacity to yield improved storm-time density predictions with the use of TLEs from only a few satellites, all which were in the same orbital plane. This differs also from the HASDM, which uses high temporal resolution drag information from the trajectories of $\sim$75 different calibration satellites at a variety of altitudes (Storz et al., 2005).

The most prominent limitation of this technique is that its sole reliance on TLE-driven orbit propagation places a limit on the power of the obtained corrections. Since TLEs are typically available once every day or two, the global corrections to F10.7 and 3-hour a_p obtained by MOA run the risk of 'smoothing over' rapid changes the density. This is most clearly observed in two ways regarding our results: the width of the peak corrected orbit-averaged densities, and the lack of distinct density features in the corrected orbit-averaged densities that are present in the orbit-averaged densities in SWARM's accelerometer-derived data, such as the second 'peak' in the density during the main phase. While individual TLEs do not provide good temporal resolution, they are nevertheless available for a plethora of orbiting objects at a wide variety of altitudes. We aim to improve MOA by determining how storm-time density modeling can be improved with this simple method by using TLEs from many more objects. We also note that at present, MOA associates the corresponding corrections to F10.7 and 3-hour a_p found for each satellite with the either noon or the beginning of the day, respectively, and then estimates corrections between those times with linear interpolation. We aim to see if improvements

in density prediction may result from associating corrections with the TLE epoch directly, taking the corrections for each satellite, and then computing new corrections by forming a univariate spline through the median corrections found across all satellites combined. This may properly "fill in the gaps", as TLEs for each satellite are not reported at the same epoch each day, allowing for any resulting index corrections to generate the distinct features in orbit-averaged density observed in accelerometer data.

Future work will involve a systematic study of MOA's capabilities across a series of catalogued geomagnetic storms that have occurred within the last decade. It will be necessary to determine the efficacy of this algorithm in handling anomalously large geomagnetic disturbances such as those characteristic of the St. Patrick's Day Storms of 2013 and 2015, and also minor disturbances such as those characteristic of March 6, 2016. It is additionally worth noting that MOA may perform differently when calculating corrections to NRLMSISE-00 or other models such as the those of the Jacchia family, and the Drag-Temperature Model. Achieving these milestones will elucidate the utility of using simple methods to address the common challenge of storm-time thermospheric density modeling and prediction.

Acknowledgments

This research was funded by the University of Michigan Rackham Merit Fellowship, NRL Grant Number N00173-18-1-G006 and by the Michigan Space Grant Consortium, NASA grant #NNX15AJ20H. We acknowledge use of NASA GSFC′s Space Physics Data Facility′s OMNIWeb service and OMNIdata, the Space Weather Prediction Center data from the National Oceanic and Atmospheric Administration, Dst data collected by the World Data Center for Geomagnetism, Kyoto operated at Kyoto University (http://wdc.kugi.kyoto-u.ac.jp/index.html), and publically available data collected by the SWARM spacecrafts from ESA (ftp://swarm-diss.eo.esa.int/Level2daily/Latest_baselines/DNS/POD/). Data used to generate in the Methodology and Results section, along with instructions on how to generate those figures, is stored on Google Drive (https://tinyurl.com/ya7b5hvf).

References

Akasofu, S. (2018). A review of the current understanding in the study of geomagnetic storms. *International Journal of Earth Science and Geophysics*, 4-18.

Brouwer, D. (1959). Solution of the problem of artificial satellite theory without drag. *The Astronomical Journal*, *64*(1274).

Bruinsma, S., Thuillier, G., & Barlier, F. (2003). The dtm-2000 empirical thermosphere model with new data assimilation and constraints at lower boundary: accuracy and properties. *Journal of Atmospheric and Solar-Terrestrial Physics*, *65*, 1053-1070.

Bruinsma, S. L., Doornbos, E., & Bowman, B. R. (2014). Validation of goce densities and evaluation of thermosphere models. *Advances in Space Research*, *54*, 576-585.

Bruinsma, S. L., Forbes, J. M., Nerem, R. S., & Zhang, X. (2006). Thermosphere density response to the 20-21 november 2003 solar and geomagnetic storm from champ and grace accelerometer data. *Journal of Geophysical Research*, *111*.

Burke, W. J., Huang, C. Y., Marcos, F. A., & Wise, J. O. (2007). Interplanetary control of thermospheric densities during large magnetic storms. *Journal of Atmospheric and Solar-Terrestrial Physics*, *69*, 279-287.

Burns, A. G., Killeen, T. L., Deng, W., Carignan, G. R., & Roble, R. G. (1995). Geomagnetic storm effects in the low- to middle-latitude upper thermosphere. *Journal of Geophysical Research*, *100*.

Bussy-Virat, C. D., Getchius, J., & Ridley, A. J. (2018). The spacecraft orbital characterization kit and its applications to the cygnss mission. *2018 Space Flight*

Mechanics Meeting, *AIAA SciTech Forum*.

Bussy-Virat, C. D., Ridley, A. J., & Getchius, J. (2018). Effects of uncertainties in the atmospheric density on the probability of collision between space objects. *Space Weather*, *16*, 510-537.

Doornbos, E., Heiner, K., & Pieter, V. (2008). Use of two-line element data for thermosphere neutral density model calibration. *Advances in Space Research*, *41*, 1115-1122.

Doornbos, E., & Klinkrad, H. (2006). Modelling of space weather effects on satellite drag. *Advances in Space Research*, *37*, 1229-1239.

Forbes, J. M., Zhang, X., & S., B. (2012). Middle and upper thermosphere density structures due to nonmigrating tides. *Journal of Geophysical Research: Space Physics*, *117*.

Gondelach, D. J., & Linares, R. (2020). Real-time thermospheric density estimation via two-line element data assimilation. *Space Weather*, *18*.

Guo, J., Feng, X., Forbes, J. M., Lei, J., Zhang, J., & Chenming, T. (2010). On the relationship between thermosphere density and solar wind parameters during intense geomagnetic storms. *Journal of Geophysical Research*, *115*(A12335).

Hoots, F. R., Jr., S., W., P., & Glover, R. A. (2004). History of analytical orbit modeling in the u.s. space surveillance system. *Journal of Guidance, Control, and Dynamics*, *27*(2).

Jacchia, L. G. (1979). Cira 1972, recent atmospheric models, and improvements in progress. *Proceedings of the Open Meetings of the Working Groups on Physical Sciences of the Twenty-First Plenary Meeting of COSPAR, Innsbruck, Austria, 29 May10 June 197*, 179-192.

Johnson, N. L. (1993). U.s. space surveillance. *Advances in Space Research*, *13*, 5-20.

Knipp, D. J., Tobiska, W. K., & Emery, B. A. (2004). Direct and indirect thermospheric heating sources for solar cycles 21-23. *Solar Physics*, *224*, 495-505.

Kozai, Y. (1959). The motion of a close earth satellite. *The Astronomical Journal*, *64*, 367.

Lane, M. H., & Cranford, K. H. (1969). An improved analytical drag theory for the artificial satellite problem. *AIAA Paper*(69-925).

Lane, M. H., & Hoots, F. R. (1979). Spacetrack report #2: General perturbation theories derived from the 1965 lane drag theory. *Aerospace Defense Command, Peterson AFB, CO*.

Liu, H., & Lhr, H. (2005). Strong disturbance of the upper thermospheric density due to magnetic storms: Champ observations. *Journal of Geophysical Research*, *110*.

Liu, H., Lhr, H., & Khler, W. (2005). Global distribution of the thermospheric total mass density derived from champ. *Journal of Geophysical Research*, *110*.

Lyddane, R. H. (1963). Small eccentricities or inclinations in the brouwer theory of the artificial satellite. *The Astronomical Journal*, *68*(8).

Mayr, H. G., Varosi, H. F., & A., H. F. (1984). Global excitation of wave phenomena in a dissipative multiconstituent medium, 2, impulsive perturbations in the earth's thermosphere. *Journal of Geophysical Research: Space Physics*, *89*.

Moe, K., M., M., & Rice, C. (2004). Simultaneous analysis of multi-instrument satellite measurements of atmospheric density. *Journal of Spacecraft and Rockets*, *41*(5).

Oliveira, D. M., Zesta, E., Schuck, P. W., & Sutton, E. K. (2017). Thermosphere global time response to geomagnetic storms caused by coronal mass ejections. *Journal of Geophysical Research: Space Physics*, *122*, 10762-10782.

Picone, J. M., Emmert, J. T., & Lean, J. L. (2005). Thermospheric densities derived from spacecraft orbits: Accurate processing of two-line element sets. *Journal of Geophysical Research: Space Physics*, *110*.

Picone, J. M., Hedin, A. E., Drob, D. P., & Aikin, A. C. (2002). Nrlmsise-00 em-

pirical model of the atmosphere: Statistical comparisons and scientific issues. *Journal of Geophysical Research: Space Physics*, *107*.

Prolss, G. W. (1993). On explaining the local time variation of ionospheric storm effects. *Annals of Geophysics*, *11*, 1-9.

Rhoden, E. A., Forbes, J. M., & A., M. F. (2000). The influence of geomagnetic and solar variabilities on lower thermosphere density. *Journal of Atmospheric and Solar-Terrestrial Physics*, *62*, 999-1013.

Ruan, H., Du, J., Cook, M., Wang, W., Yue, J., Gan, Q., ... Lei, J. (2015). A numerical study of the effects of migrating tides on thermispheric midnight density maximum. *Journal of Geophysical Research: Space Physics*, *120*, 6766-6778.

Storz, M. F., Bowman, B. R., Branson, M. J. I., Casali, S. J., & Tobiska, W. K. (2005). High accuracy satellite drag model (hasdm). *Advances in Space Research*, *36*, 2497-2505.

Sutton, E. K., Forbes, J. M., & Knipp, D. J. (2009). Rapid response of the thermosphere to variations in joule heating. *Journal of Geophysical Research*, *114*.

Vallado, D. A., & Crawford, P. (2008). Sgp4 orbit determination. *AIAA/AAS Astrodynamics Specialist Conference*, *AIAA 2008-6770*.

Vallado, D. A., Crawford, P., Husjak, R., & Kelso, T. S. (2006). Revisiting spacetrack report #3. *Astrodynamics Specialist Conference*.

Vichare, G., & Lakhina, G. S. (2005). Some characteristics of intense geomagnetic storms and their energy budget. *Journal of Geophysical Research*, *110*.

Vickers, H., Kosch, M. J., Sutton, E., Bjoland, L., Ogawa, Y., & La Hoz, C. (2014). A solar cycle of upper thermosphere density observations from the eiscat svalbard radar. *Journal of Geophysical Research: Space Physics*, *119*, 6833-6845.

Wang, Z., Hu, Q., Zhong, Q., & Y., W. (2018). Linear multistep f10.7 forecasting based on task correlation and heteroscedasticity. *Earth and Space Science*, *5*, 863-874.

Wrenn, G. L. (1987). Time-weighted accumulations ap(z) and kp(z). *Journal of Geophysical Research*(A9), 10,125 - 10,129.

Figure 4.

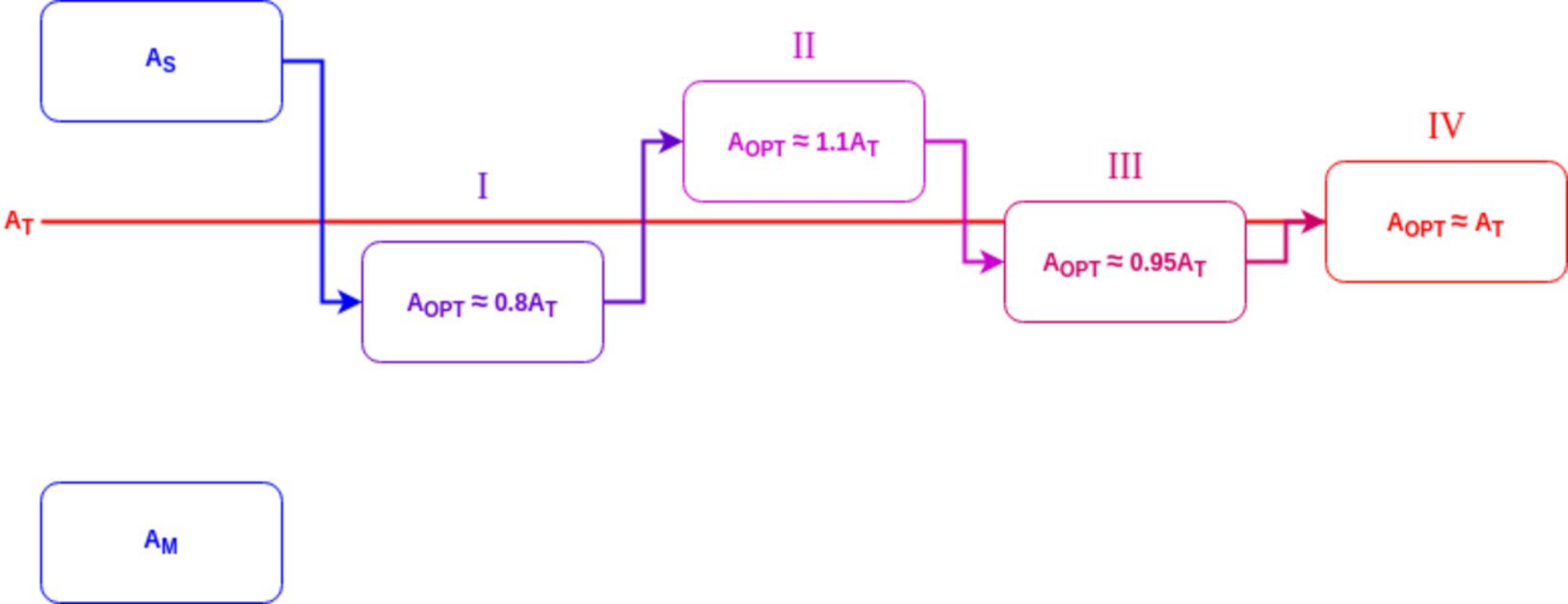
A_S
II
$A_{OPT} \approx 1.1A_T$
IV
III
I
A_T
$A_{OPT} \approx A_T$
$A_{OPT} \approx 0.95A_T$
$A_{OPT} \approx 0.8A_T$
A_M

Figure 8b.

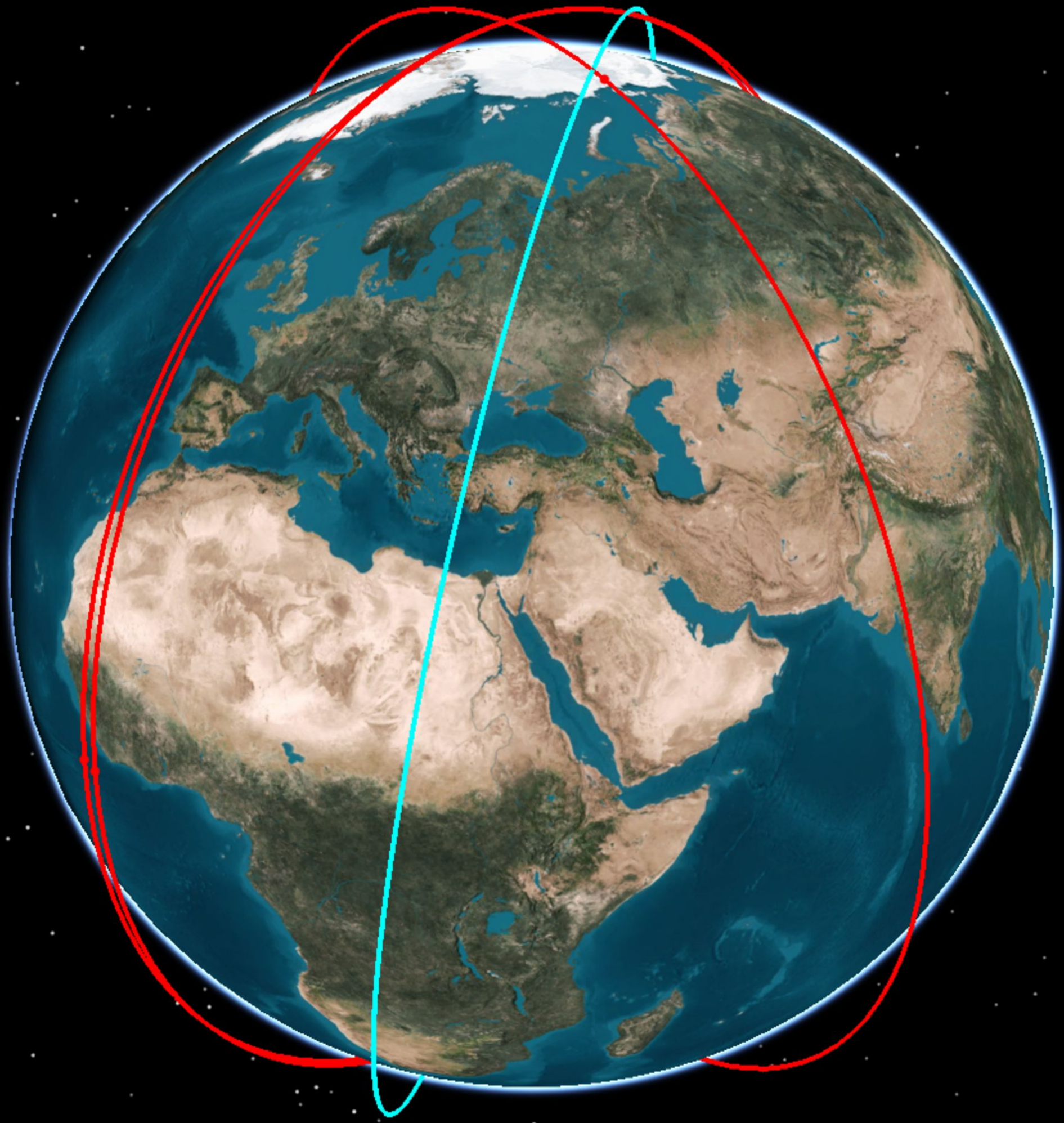

Earth Inertial Axes

26 May 2017 08:00:00.000 Time Step: 10.00 sec

Figure 8a.

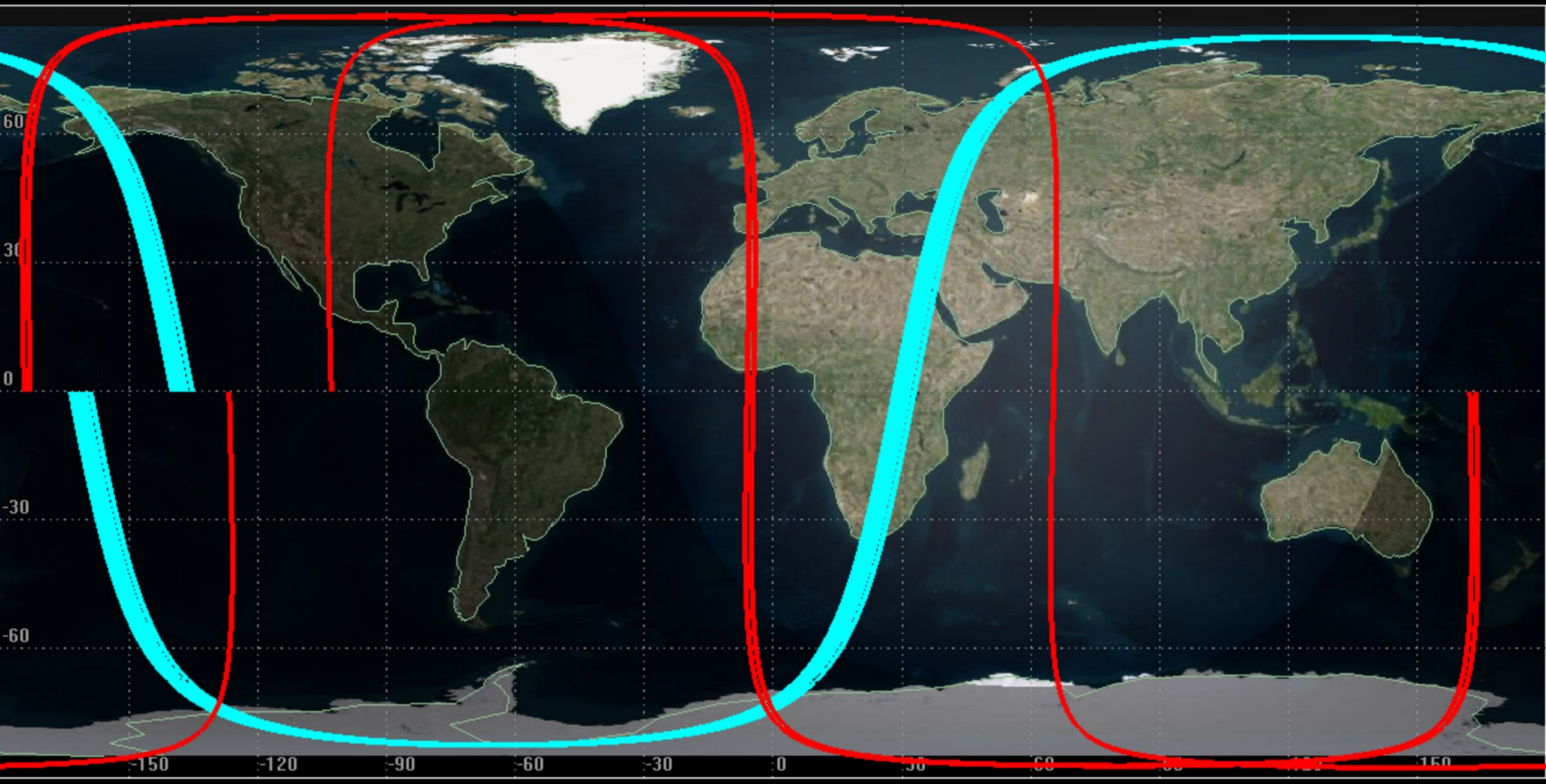

Figure 5.

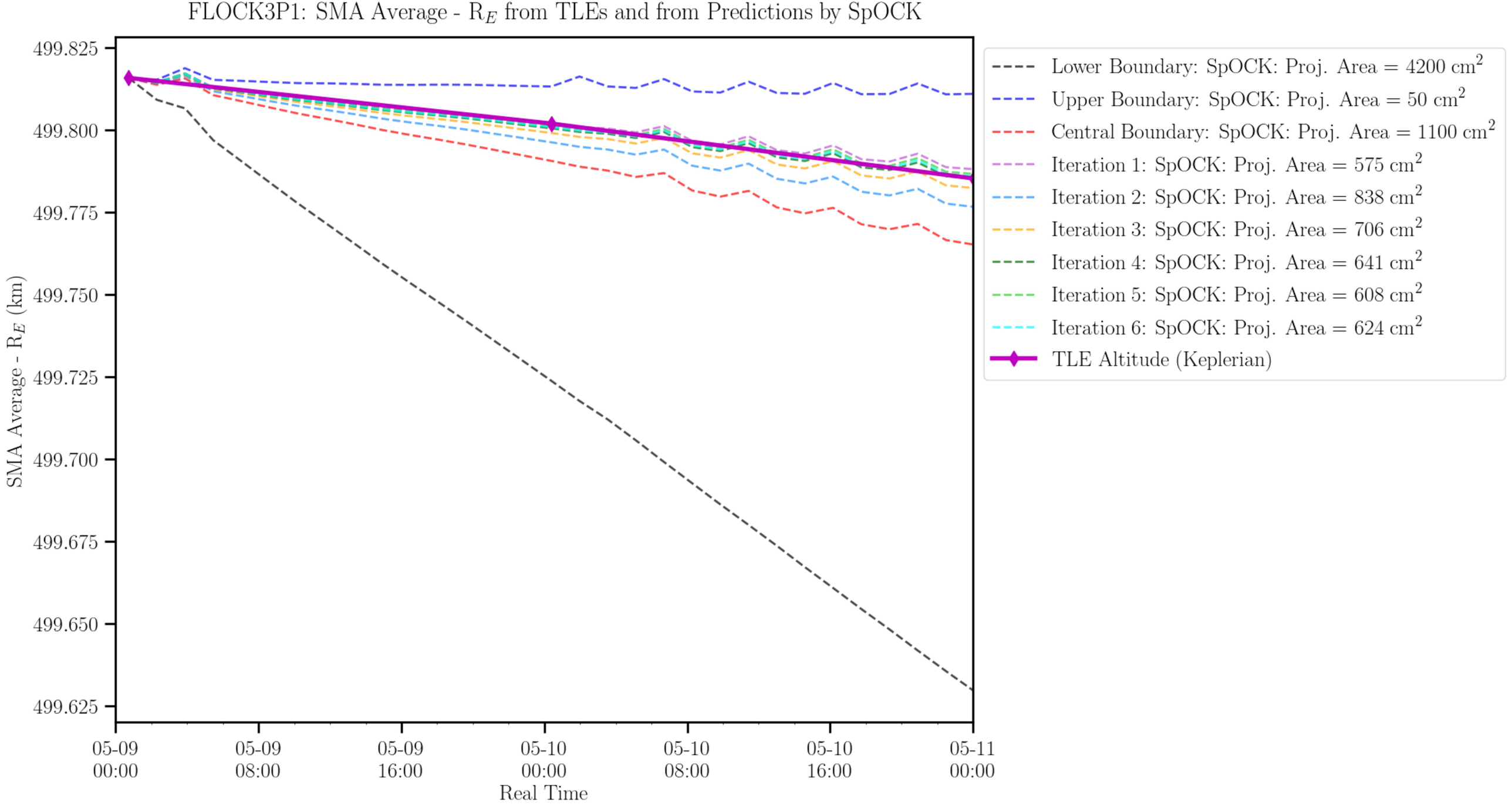
FLOCK3P1: SMA Average - R_E from TLEs and from Predictions by SpOCK
SMA Average - R_E (km)
499.825
499.800
499.775
499.750
499.725
499.700
499.675
499.650
499.625
05-09 00:00
05-09 08:00
05-09 16:00
05-10 00:00
05-10 08:00
05-10 16:00
05-11 00:00
Real Time
Lower Boundary: SpOCK: Proj. Area = 4200 cm^2
Upper Boundary: SpOCK: Proj. Area = 50 cm^2
Central Boundary: SpOCK: Proj. Area = 1100 cm^2
Iteration 1: SpOCK: Proj. Area = 575 cm^2
Iteration 2: SpOCK: Proj. Area = 838 cm^2
Iteration 3: SpOCK: Proj. Area = 706 cm^2
Iteration 4: SpOCK: Proj. Area = 641 cm^2
Iteration 5: SpOCK: Proj. Area = 608 cm^2
Iteration 6: SpOCK: Proj. Area = 624 cm^2
TLE Altitude (Keplerian)

Figure 6.

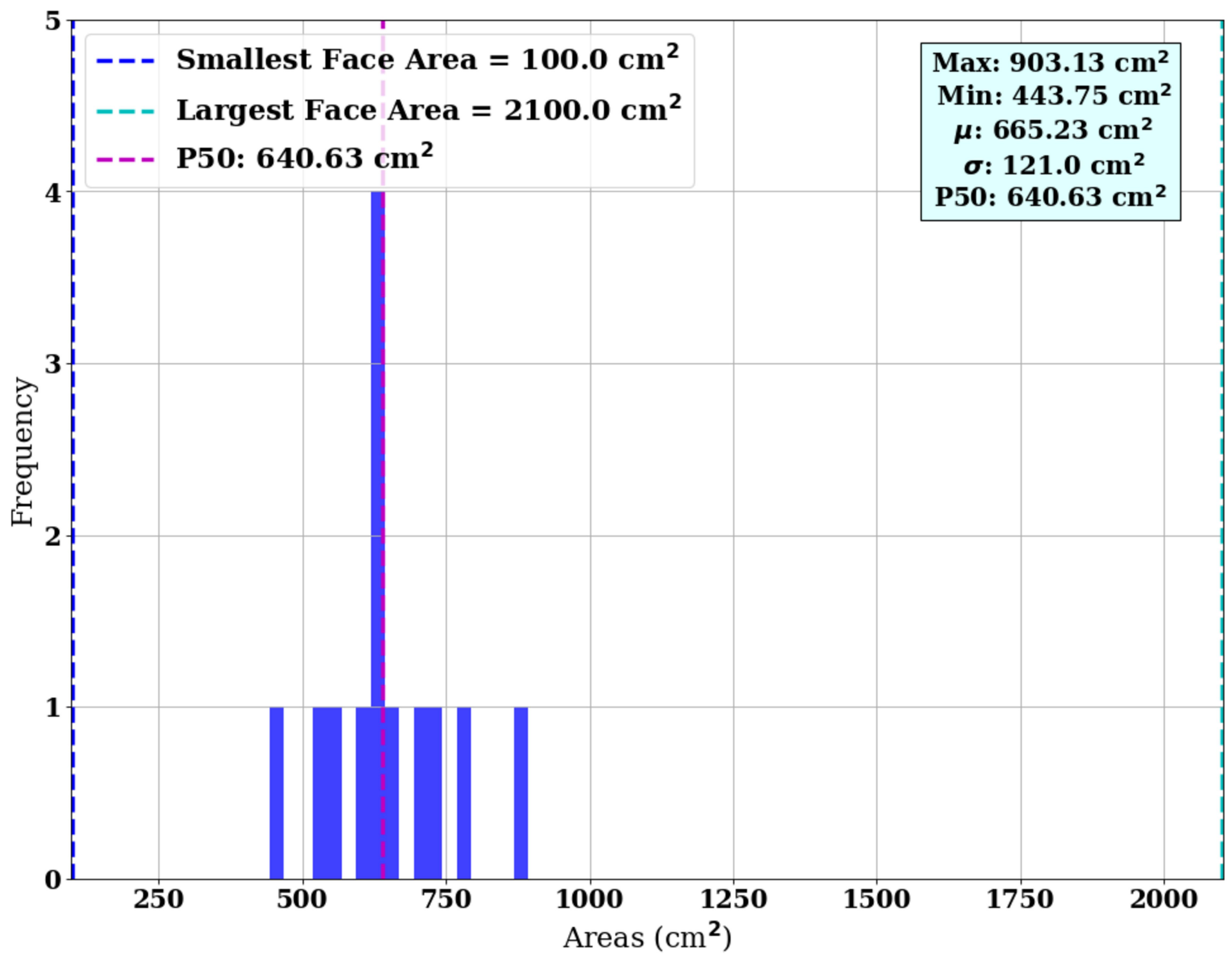
Smallest Face Area = 100.0 cm²
Largest Face Area = 2100.0 cm²
P50: 640.63 cm²
Max: 903.13 cm²
Min: 443.75 cm²
μ: 665.23 cm²
σ: 121.0 cm²
P50: 640.63 cm²
Frequency
Areas (cm²)
0
1
2
3
4
5
250
500
750
1000
1250
1500
1750
2000

Figure 10.

AROPT Histograms: 2017-05-09 - 2017-05-24 (10 satellites)

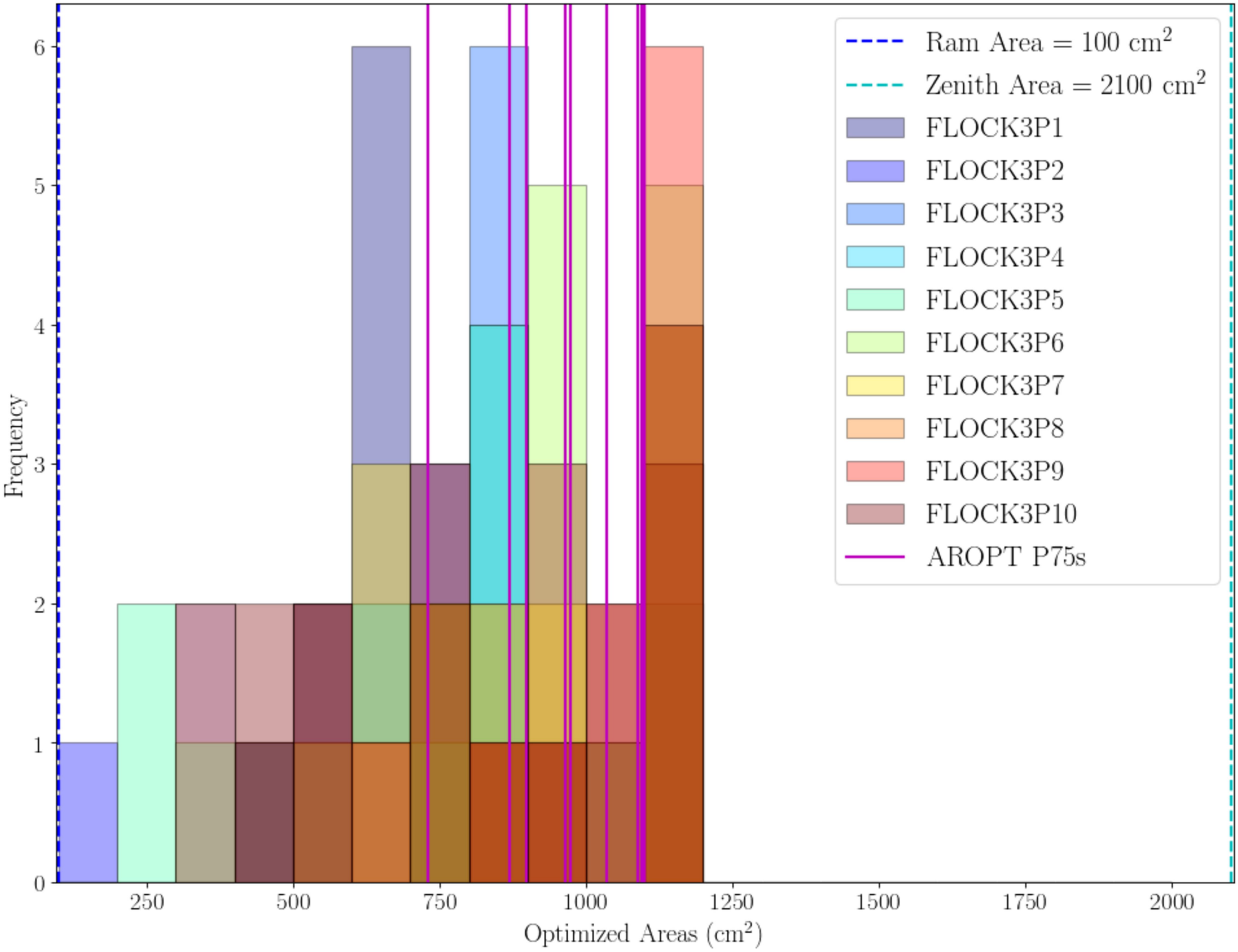

Figure 1 (top).

dSMA/dt (km/year)

10
0
−10
20
30
−40
−50

20
0
−20
−40
−60
−80
−100
−120
−140
−160

Dst (nT)

08-16 00:00
08-17 22:12
08-19 20:24
08-21 18:36
08-23 16:48
08-25 15:00
08-27 13:12
08-29 11:24
08-31 09:36
09-02 07:48
09-04 06:00

Real Time

Time-Averaged Kyoto Dst

Linear Interpolation

Time-Averaged dSMA/dt

Figure 1 (bottom).

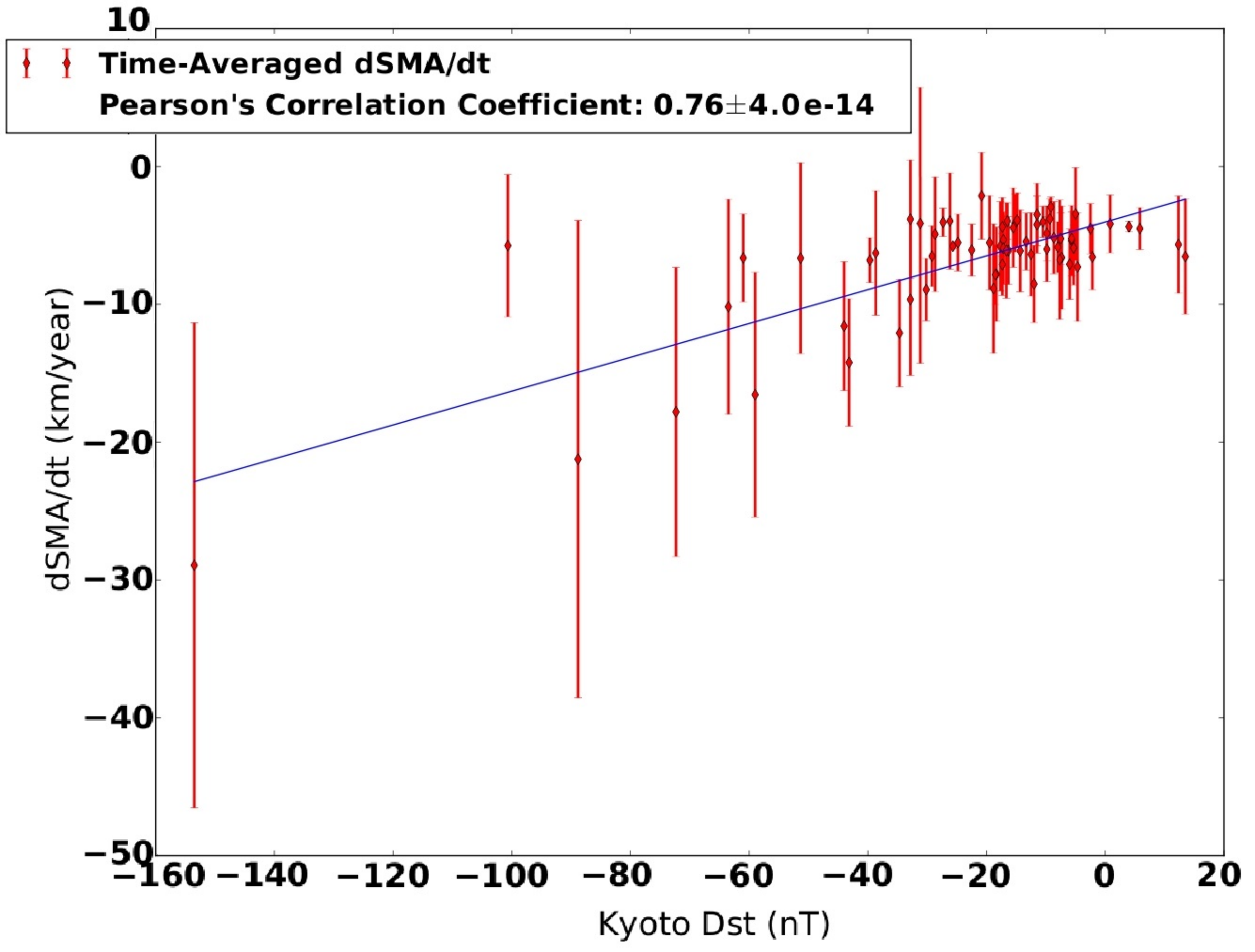
Time-Averaged dSMA/dt
Pearson's Correlation Coefficient: 0.76±4.0e-14
dSMA/dt (km/year)
10
0
−10
−20
−30
−40
−50
−160
−140
−120
−100
−80
−60
−40
−20
0
20
Kyoto Dst (nT)

Figure 12.

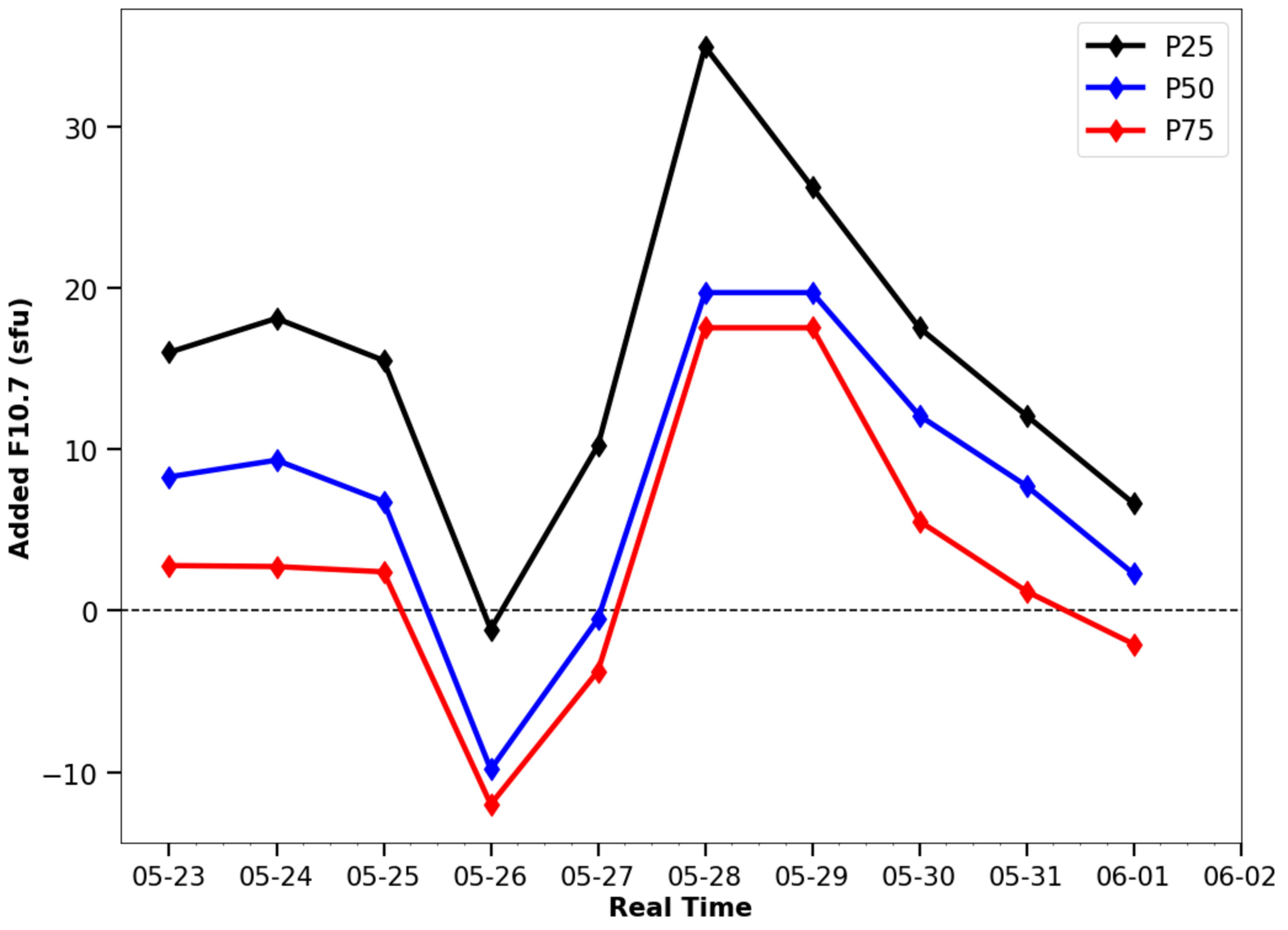
P25
P50
P75
30
20
10
0
−10
Added F10.7 (sfu)
05-23
05-24
05-25
05-26
05-27
05-28
05-29
05-30
05-31
06-01
06-02
Real Time

Figure 7.

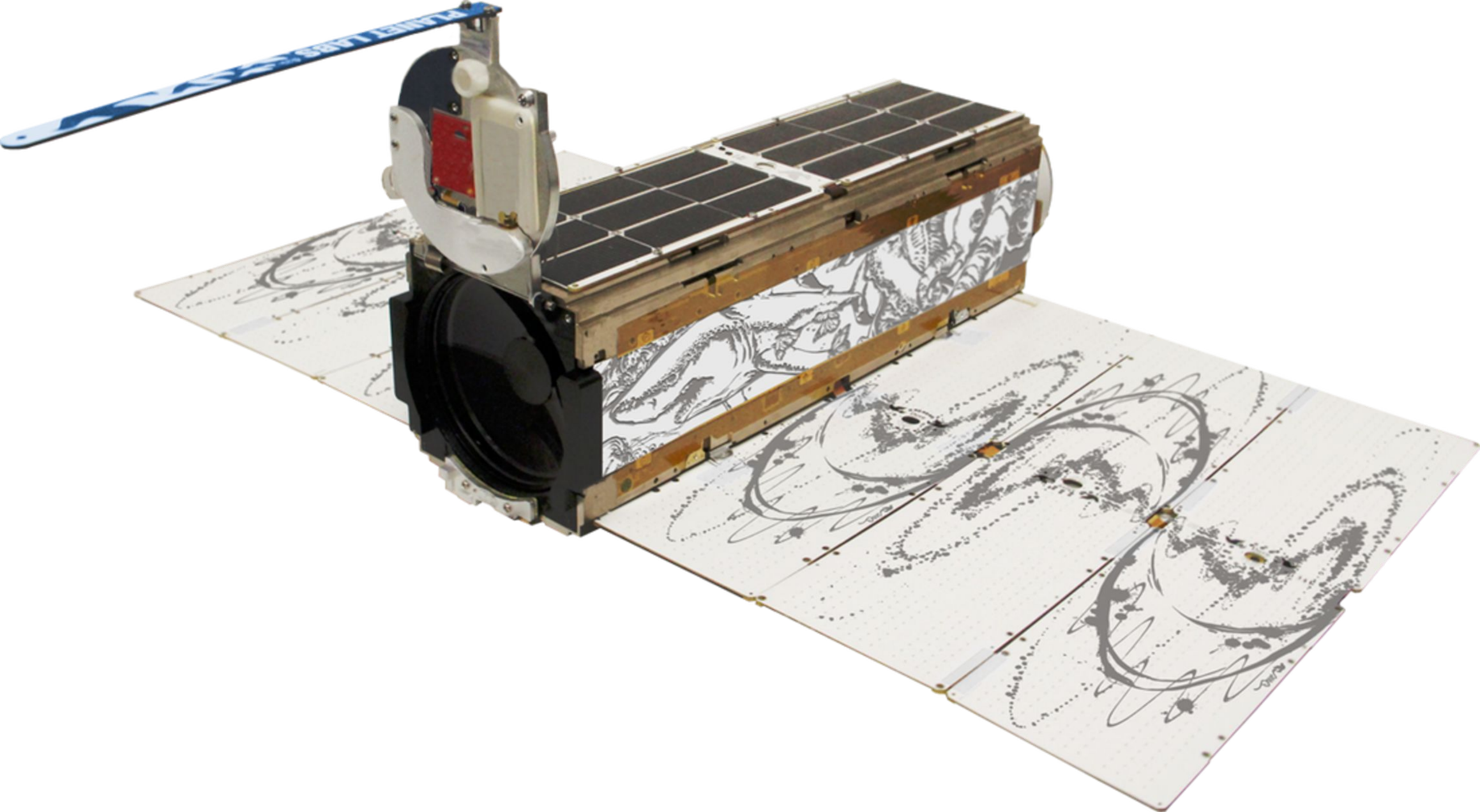
PLANET LABS

Figure 11.

Static and Linearly-interpolated F10.7 Corrections: 2017-05-23 - 2017-06-02 (10 satellites)

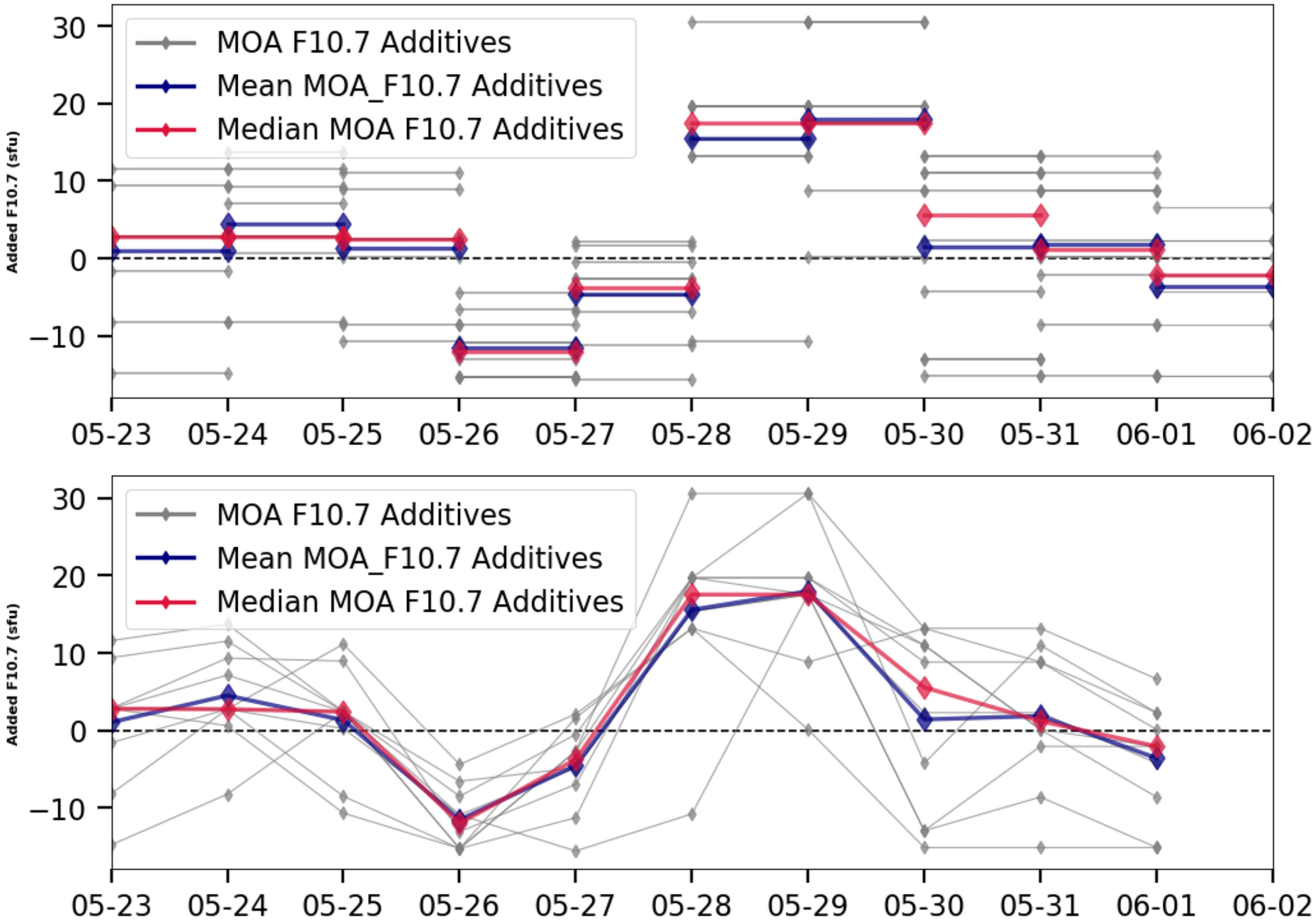

Figure 9c.

dSMA (km/year)

25
20
15
10
5
0

05-23
05-24
05-25
05-26
05-27
05-28
05-29
05-30
05-31
06-01
06-02

Figure 13.

OMNIWeb 3-hr a_p
MOA OMNIWeb 3-hr a_p
Median MOA 3-hr a_p Corrections
OMNIWeb F10.7
MOA F10.7
Median MOA F10.7 Corrections
F10.7 (sfu)
3-hr a_p (nT)
100
80
60
40
20
0
−20
140
120
100
80
60
40
20
0
05-23
05-24
05-25
05-26
05-27
05-28
05-29
05-30
05-31
06-01
06-02
Real Time

Figure 3.

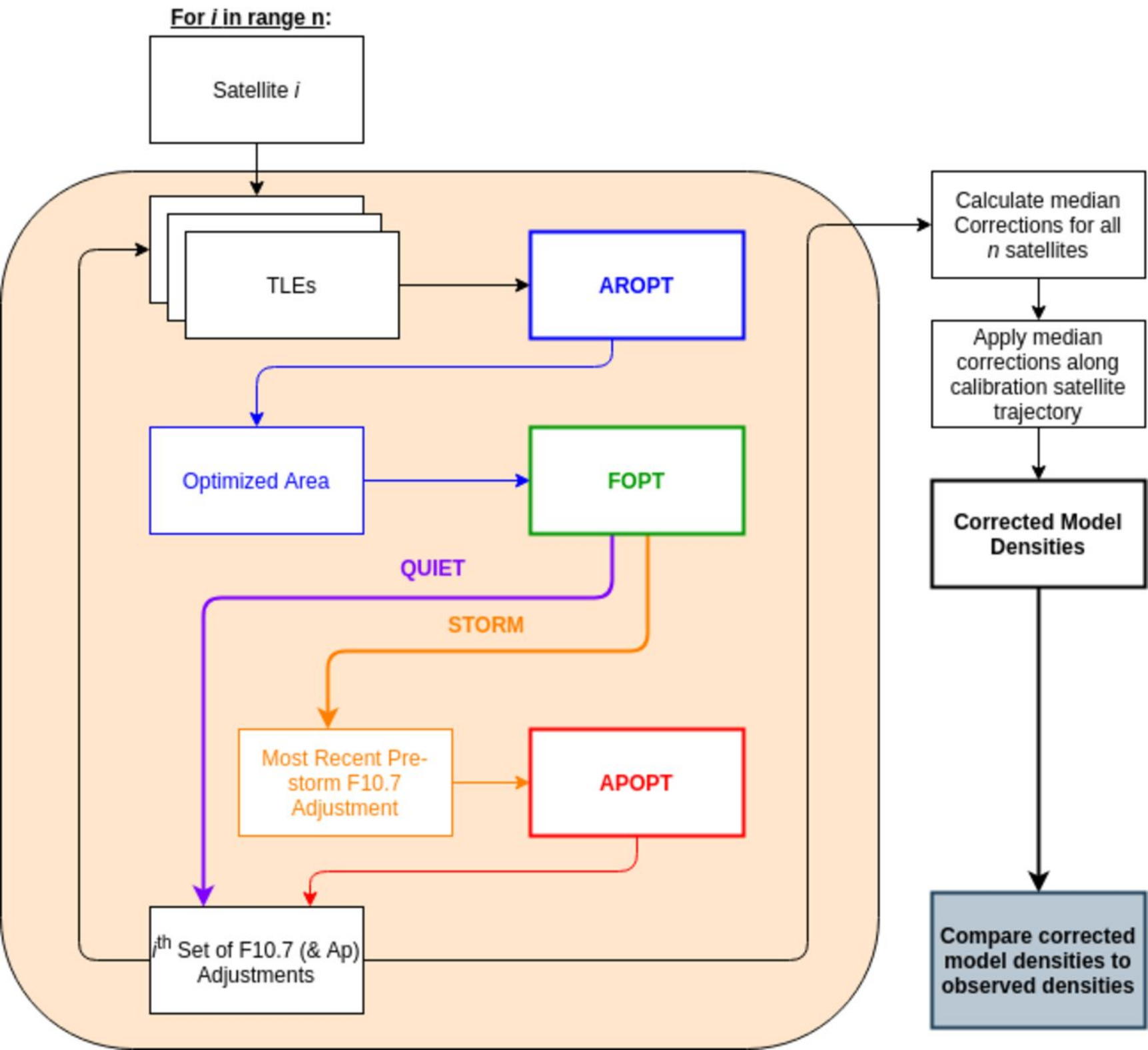
For *i* in range n:
Satellite *i*
TLEs
AROPT
Optimized Area
FOPT
QUIET
STORM
Most Recent Pre-storm F10.7 Adjustment
APOPT
i^{th} Set of F10.7 (& Ap) Adjustments
Calculate median Corrections for all *n* satellites
Apply median corrections along calibration satellite trajectory
Corrected Model Densities
Compare corrected model densities to observed densities

Figure 9a.

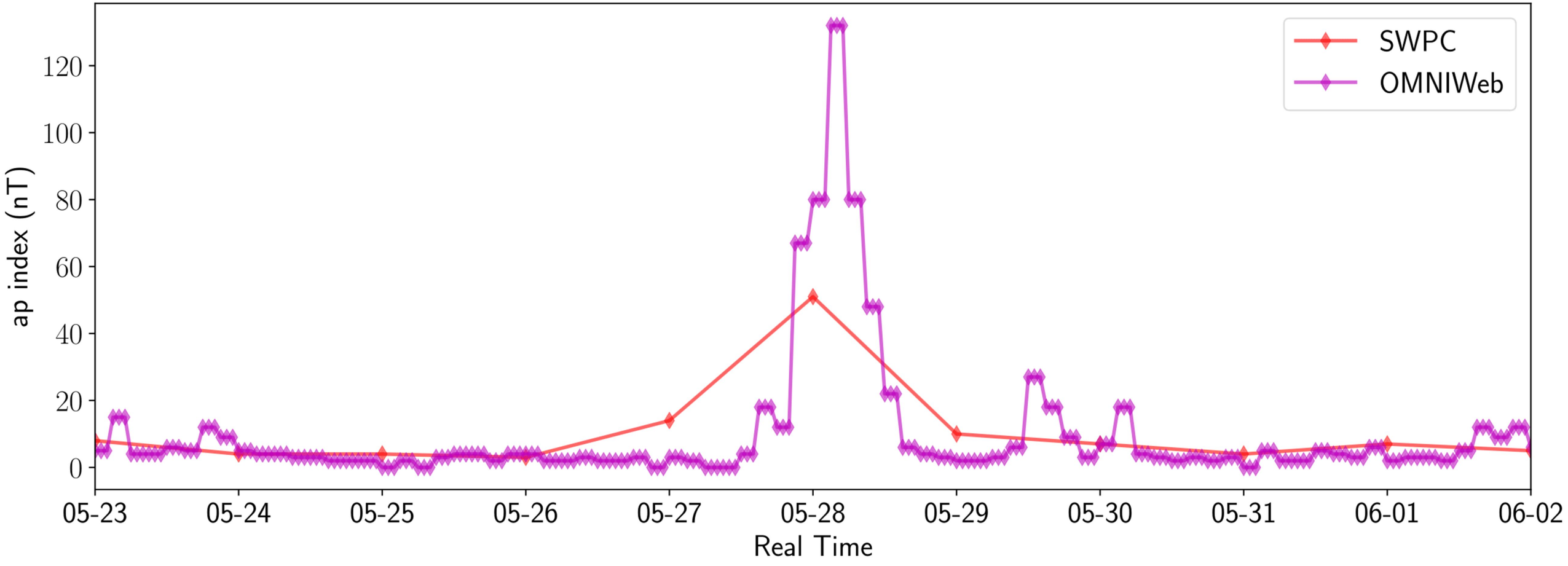
SWPC
OMNIWeb
ap index (nT)
0
20
40
60
80
100
120
05-23
05-24
05-25
05-26
05-27
05-28
05-29
05-30
05-31
06-01
06-02
Real Time

Figure 9b.

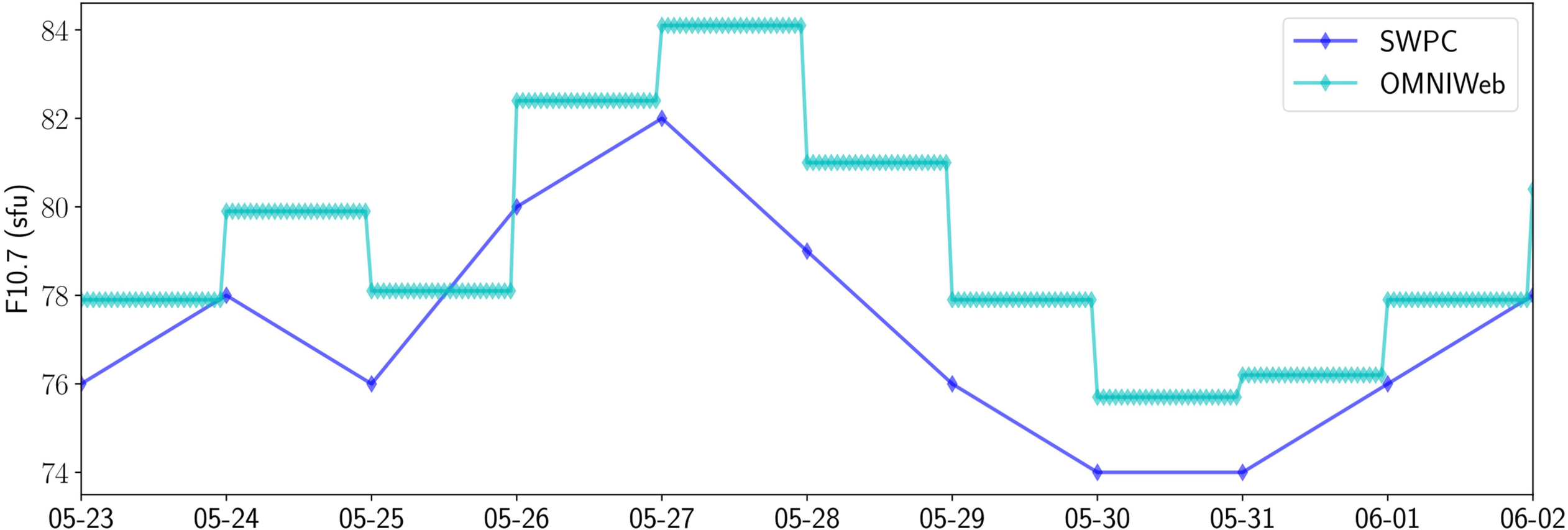
F10.7 (sfu)
84
82
80
78
76
74
05-23
05-24
05-25
05-26
05-27
05-28
05-29
05-30
05-31
06-01
06-02
SWPC
OMNIWeb

Figure 2.

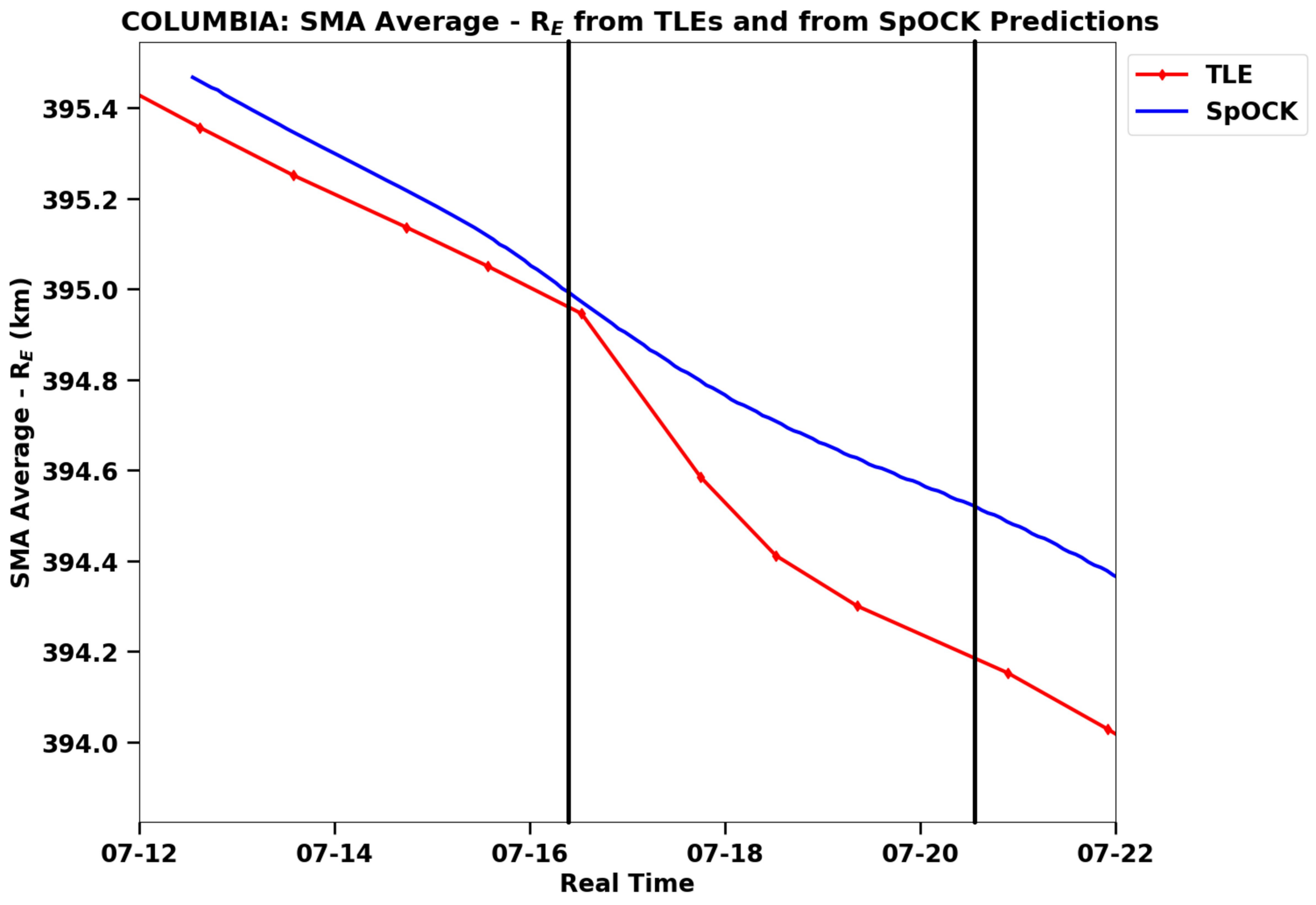
COLUMBIA: SMA Average - R_E from TLEs and from SpOCK Predictions
TLE
SpOCK
395.4
395.2
395.0
394.8
394.6
394.4
394.2
394.0
SMA Average - R_E (km)
07-12
07-14
07-16
07-18
07-20
07-22
Real Time

Figure 14a.

SWARM-A: Orbit-averaged Neutral Densities 2017-05-23 - 2017-06-02

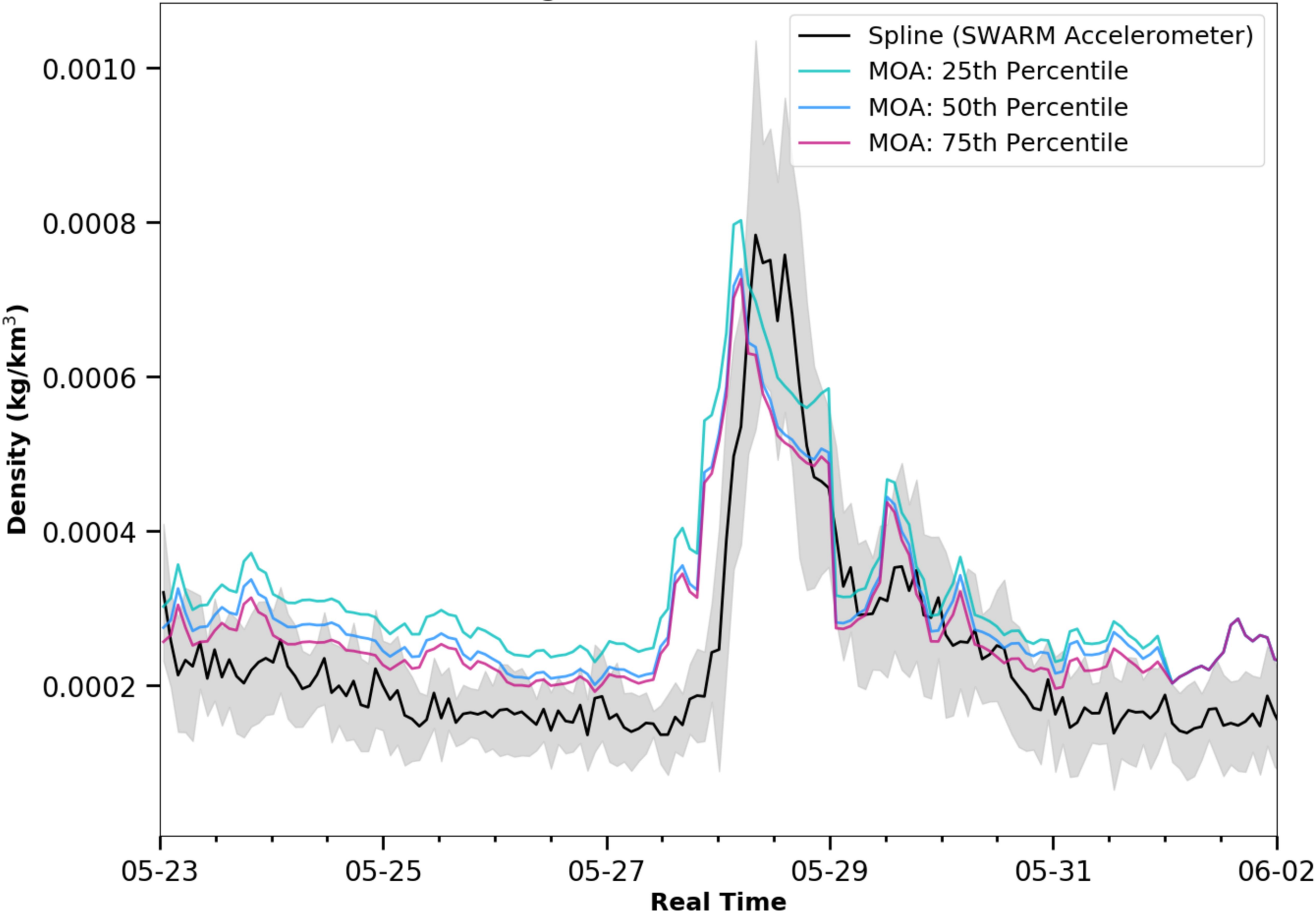

Figure 15a.

SWARM-A: Orbit-averaged Neutral Densities 2017-05-23 - 2017-06-02

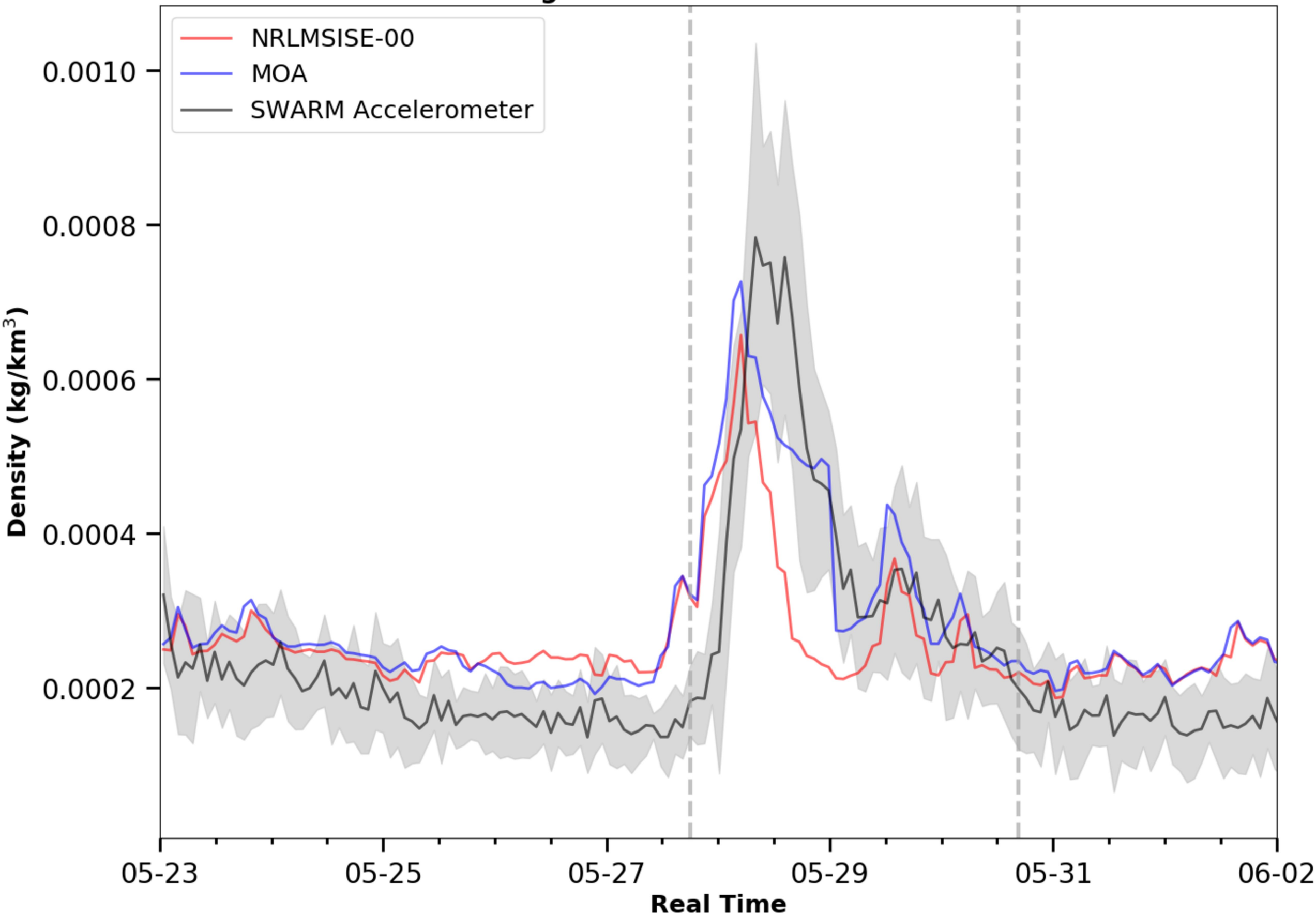

Figure 14b.

SWARM-B: Orbit-averaged Neutral Densities 2017-05-23 - 2017-06-02

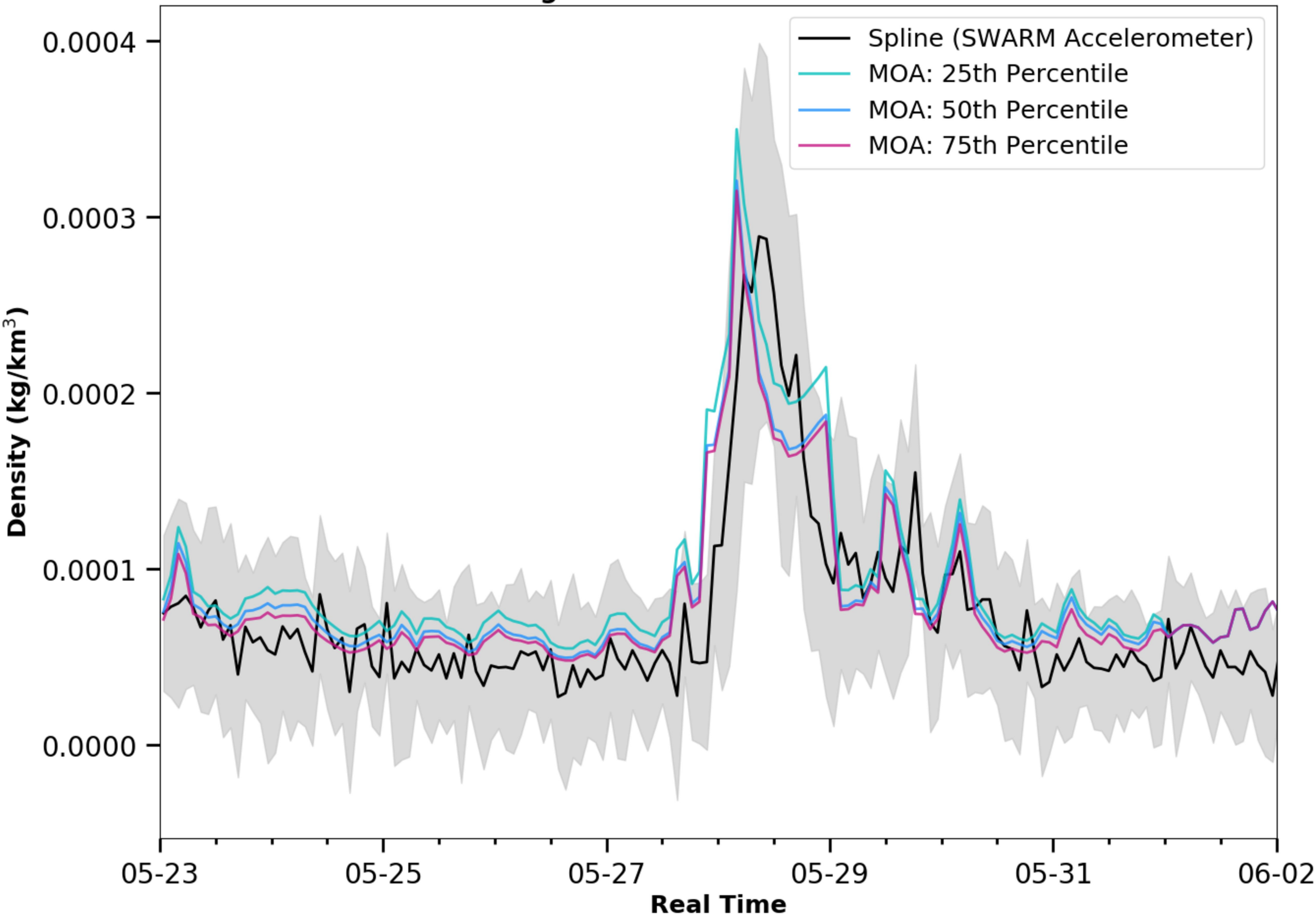

Figure 15b.

SWARM-B: Orbit-averaged Neutral Densities 2017-05-23 - 2017-06-02